Bioactive Materials 48 (2025) 493–509

Contents lists available at ScienceDirect

Bioactive Materials

journal homepage: www.keaipublishing.com/en/journals/bioactive-materials

A micro-metabolic rewiring assay for assessing hypoxia-associated cancer metabolic heterogeneity

Jeong Min Oh [a], Tianze Guo [a], Hydari Masuma Begum [a], Saci-Elodie Marty [a], Liang Sha [b], Cem Kilic [a], Hao Zhou [a], Yali Dou [b,c], Keyue Shen [a,c,d,1,*]

[a] Department of Biomedical Engineering, University of Southern California, Los Angeles, CA, 90089, USA
[b] Department of Medicine, Keck School of Medicine, University of Southern California, Los Angeles, CA, 90033, USA
[c] Norris Comprehensive Cancer Center, University of Southern California, Los Angeles, CA, 90033, USA
[d] USC Stem Cell, University of Southern California, Los Angeles, CA, 90033, USA

ARTICLE INFO

Keywords:
Metabolic rewiring
Hypoxia
Tumor heterogeneity
Metabolism-targeting therapy
Tumor microenvironment

ABSTRACT

Cancer metabolism plays an essential role in therapeutic resistance, where significant inter- and intra-tumoral heterogeneity exists. Hypoxia is a prominent driver of metabolic rewiring behaviors and drug responses. Recapitulating the hypoxic landscape in the tumor microenvironment thus offers unique insights into heterogeneity in metabolic rewiring and therapeutic responses, to inform better treatment strategies. There remains a lack of scalable tools that can readily interface with imaging platforms and resolve the heterogeneous behaviors in hypoxia-associated metabolic rewiring. Here we present a micro-metabolic rewiring (μMeRe) assay that provides the scalability and resolution needed to characterize the metabolic rewiring behaviors of different cancer cells in the context of hypoxic solid tumors. Our assay generates hypoxia through cellular metabolism without external gas controls, enabling the characterization of cell-specific intrinsic ability to drive hypoxia and undergo metabolic rewiring. We further developed quantitative metrics that measure the metabolic plasticity through phenotypes and gene expression. As a proof-of-concept, we evaluated the efficacy of a metabolism-targeting strategy in mitigating hypoxia- and metabolic rewiring-induced chemotherapeutic resistance. Our study and the scalable platform thus lay the foundation for designing more effective cancer treatments tailored toward specific metabolic rewiring behaviors.

1. Introduction

Despite substantial advancements in cancer diagnosis and treatments, therapeutic resistance remains a major threat to cancer patients [1]. Metabolic alterations are a hallmark of cancer and an essential player in mediating resistance to various therapies [2]. While new treatment strategies aiming at cancer metabolism are on the rise [3], it is increasingly recognized that different cancers have different metabolic preferences and dependencies, as illustrated by recent metabolic/metabolomic analyses and functional genomic studies [4–6]. Within the same tumors, metabolic phenotypes are also heterogeneous and plastic [7], determined by both intrinsic factors (e.g., cell origin and mutations) and extrinsic factors from the tumor microenvironment (TME) and body system (e.g., oxygen, nutrients, stromal cells, extracellular matrix or ECM, and cytokines) [8], which give rise to stress-evading and therapy-resistant cancer phenotypes [9,10]. Therefore, capturing the inter- and intra-tumoral heterogeneity in metabolic phenotypes is crucial for understanding patients' diverse responses to cancer therapy and developing more effective, personalized treatment strategies [11].

Hypoxia is a prominent driver of metabolic pathways and rewiring associated with therapeutic resistance, such as oxidative stress, cell cycle arrest, and genomic instability [12–14]. Solid tumors develop hypoxia due to an imbalance between oxygen consumption by cancer cells and limited oxygen supply by diffusion through the irregularly formed tumor vasculature [15]. As a result, oxygen levels in a solid tumor are heterogeneous and exist in a gradient, ranging from physioxic to anoxic levels [16]. Consequently, cancer cells rewire their metabolism to adapt

Peer review under the responsibility of KeAi Communications Co., Ltd.
* Corresponding author. Department of Biomedical Engineering, University of Southern California, Los Angeles, CA, 90089, USA.
E-mail address: keyue.shen@usc.edu (K. Shen).
[1] Lead contact.

https://doi.org/10.1016/j.bioactmat.2025.02.030
Received 2 November 2024; Received in revised form 11 January 2025; Accepted 19 February 2025

locally to oxygen availability. In severely hypoxic regions, cancer cells switch from oxidative phosphorylation (OXPHOS) to the oxygen-independent glycolytic pathway to maintain ATP production (Fig. 1A) [17,18], which contributes to tumor acidosis and promotes drug-resistant, malignant phenotypes [19,20]. Notably, the development of such a hypoxic landscape and its influence on therapy resistance may also vary between cancer types and subtypes, and among different patients (Fig. 1B) [16,21]. Therefore, recapitulating the hypoxic landscape of solid tumors provides a unique opportunity for revealing the inter- and intra-tumoral heterogeneity in the metabolic rewiring and therapeutic resistance.

There remains a lack of tools for characterizing the heterogeneous behaviors in hypoxia-associated metabolic rewiring [22]. In vivo tumor models may recapitulate tumor hypoxia in the most relevant manner [23]. However, it is technically challenging to study the heterogeneous and dynamic interplays within a living system. In vivo models also face high variability and low throughput, which make them unfavorable for characterizing diverse cancer types, especially in the early-stage biological investigations and preclinical therapeutic screenings. In vitro models can reveal heterogeneity in a consistent, interpretable manner and are scalable for higher throughput assays. Among those, hypoxic chambers are the most commonly used to study hypoxic signaling. However, they fail to reproduce intra-tumoral metabolic heterogeneity and disregard the inter-tumoral heterogeneity in their intrinsic ability to drive hypoxia and metabolic rewiring [24,25]. Conventional tumor spheroids, while capable of reproducing cancer cell-driven hypoxic landscapes, are technically difficult to interface with live imaging-based analysis to resolve the heterogeneous and dynamic behaviors in metabolic rewiring [26]. Overall, the existing hypoxia approaches are not suitable for assessing the cancer cell's intrinsic ability to drive hypoxia and generate different metabolic phenotypes.

Here, we present a micro-metabolic rewiring (μMeRe) assay that measures the metabolic rewiring behaviors of diverse cancer cells/types in the context of hypoxic solid tumors. Our μMeRe assay fulfills the need for a highly scalable tumor model that is compatible with high-resolution imaging and can readily capture inter- and intra-tumoral heterogeneity through the interplay between hypoxia and metabolic rewiring. Cancer cells are cultured in a hypoxia-inducing μMeRe device that recapitulates the natural process of how hypoxia is established in solid tumors. Combined with a workflow of phenotypic and gene expression analyses and quantitative measurements, the assay provides the scalability and throughput necessary for evaluating the heterogeneity of different cancer cells in driving a hypoxic TME and undergo metabolic rewiring. As a proof-of-concept, we evaluated the efficacy of a metabolism-targeting strategy in mitigating hypoxia- and metabolic rewiring-induced chemotherapeutic resistance. Our study and the scalable platform thus lay the foundation for designing more effective personalized cancer medicine aiming at metabolic rewiring in the TME.

2. Results

2.1. Designing a μMeRe assay to measure cancer-specific response to an oxygen-limited TME

To highlight the distinct metabolic rewiring characteristics of different cancer cells and/or types, we designed a micro-metabolic rewiring (μMeRe) assay to impose an oxygen-limited microenvironment on cancer cell cultures (Fig. 1C). The core of the assay is a hypoxia-inducing cell culture device (i.e., a μMeRe device) consisting of a circular micropattern of cancer cells sandwiched between two oxygen diffusion barriers (polycarbonate, or PC, at the top and glass at the bottom) [27]. A natural oxygen gradient is established across the cancer micropattern due to cell-specific consumption and limited lateral diffusion of oxygen across the monolayer (Fig. 1C). This metabolism-driven approach recapitulates the natural process of how cancer cells establish hypoxia in solid tumors, whereas the spatial patterns of metabolic profiles and rewiring dynamics are dependent on the intrinsic characteristics of the cancer cells of interest. To control for the oxygen condition, for each μMeRe assay, we also cultured cancer cells in a normoxia device in parallel. The normoxia device shares the same dimensions as the μMeRe device except without the PC oxygen diffusion barrier, thus with unobstructed oxygen supply through polydimethylsiloxane (PDMS) from above (Fig. 1D). Cancer cells in the μMeRe device establish a hypoxic landscape by oxygen consumption during cellular metabolism; in turn, they also rewire their metabolism to adapt to the new hypoxic landscape. The changes in protein markers and gene expression can then be measured as indicators of metabolic rewiring for the specific cancer cells/types (Fig. 1D).

The μMeRe device was assembled following a simple workflow using soft lithography and low-cost fabrication tools (Fig. 1E), and cancer cells were subsequently loaded through liquid-pinning to form a micropattern [27] (Fig. 1F). Materials and fabrication tools for the device are all commercially available through the mass consumer market, making it much more cost-effective compared to the conventional photolithography-based microfabrication methods. We used high-resolution micro-milling to fabricate the master mold for the PDMS component of the device, where the number, size, and shape of cancer micropatterns can be readily varied to accommodate different contexts and applications [28] (Fig. 1G). Notably, arrays of μMeRe and normoxia devices can be integrated with commercial single-well or multi-well plates to facilitate handling and enhance throughput (Fig. 1H). Overall, the design of the μMeRe device and its enhanced throughput allow for measuring the metabolic rewiring behaviors of diverse cancer cells/types in the context of hypoxic solid tumors.

2.2. μMeRe assay reveals intertumoral heterogeneity in hypoxia marker expression

To develop a μMeRe assay and examine whether it can discriminate the heterogeneous metabolic rewiring characteristics of different types of cancer cells, we cultured a panel of 8 human cancer cell lines originating from 4 different organs (ovary, prostate, lung, and breast) in μMeRe devices and their normoxia counterparts/controls (Fig. 2A). After 24 h of culture, we measured the hypoxic landscapes and rewired metabolic status established by each cancer cell type through BioTracker™ hypoxia dye (an exogenous marker for hypoxia) and immunostaining of Glut-1 (an endogenous marker for glycolysis) (Fig. 2A). The BioTracker hypoxia dye is a hypoxia-selective probe that becomes fluorescent in hypoxic cells, while Glut-1 is a glucose transporter regulated by hypoxia-inducible factor-1 (HIF-1) to facilitate anaerobic glycolysis in response to reduced oxidative phosphorylation (OXPHOS) [21]. As indicated by the BioTracker hypoxia dye, all cancer cells established a hypoxic gradient within the μMeRe device, with the greatest fluorescence intensity observed at the center of the cancer micropatterns (Fig. 2A). The hypoxic landscape and metabolic rewiring were characterized as **1)** the fold changes in the fluorescence intensities of BioTracker hypoxia dye and Glut-1 at the center of the μMeRe device versus its normoxic counterpart (Fig. 2B–D), and **2)** the radial cutoff distance of the fluorescence signal (defined as a 30% drop from the peak fluorescence at the center) in the μMeRe device (Fig. 2C–E). These measurements offer an understanding of the magnitude and extent of cancer cells influenced by the oxygen-limited microenvironment and their corresponding metabolic rewiring behaviors.

Interestingly, cancer cells originating from the same organ showed a similar level of increase in the fluorescence of hypoxia dye in μMeRe devices over their normoxia controls (Fig. 2B). Among different cancer types, the two prostate cancer cells, LNCaP and PC3, showed the highest change (>3.5-fold), while the ovarian cancer cells, OAW42 and SKOV3, had the lowest (~1.9-fold). The cutoff distance varied across the panel of cancer cells, with the LNCaP prostate cancer cells (~2692 μm) and the SKOV3 ovarian cancer cells (~1682 μm) at the two ends of the distribution (Fig. 2C). Since the radius of cancer micropatterns was fixed at

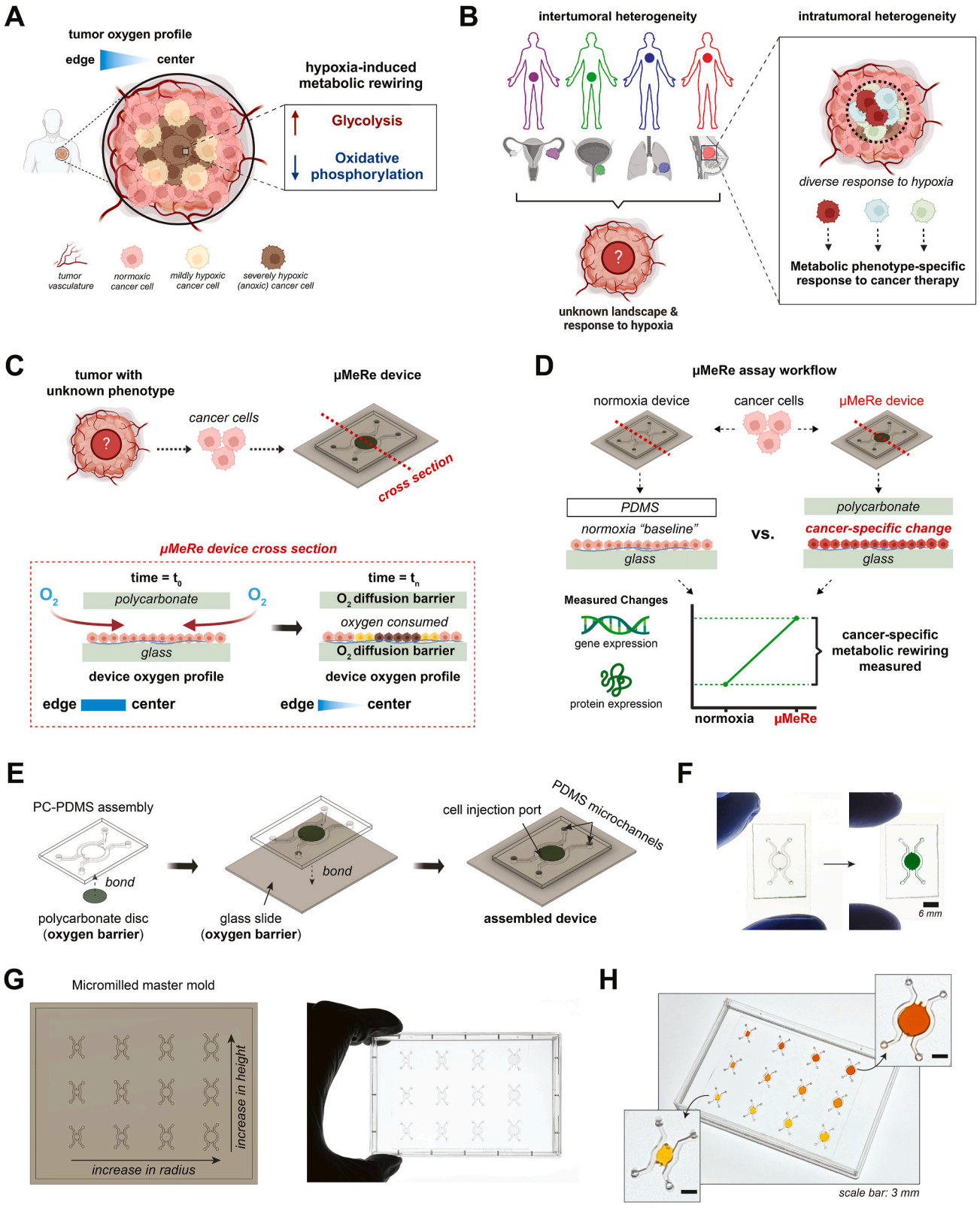

Fig. 1. Capturing tumor heterogeneity under an oxygen-limited microenvironment in the μMeRe device. **(A)** A schematic of the hypoxic profile and associated metabolic rewiring in the tumor microenvironment in solid tumors. **(B)** Inter- and intra-tumoral heterogeneity and the corresponding distinct therapeutic responses. **(C)** A schematic of the μMeRe device and the working mechanism of establishing a hypoxia gradient. **(D)** The workflow of a μMeRe assay. Cancer cells are cultured in a μMeRe device and a normoxia control device. Cancer cells in the μMeRe device establish a hypoxia landscape through oxygen consumption and adaptive metabolic rewiring response. Hypoxia markers and gene expression are measured and compared for the specific cancer cells. **(E)** The μMeRe device fabrication process. **(F)** An assembled μMeRe device. The tumor region is highlighted by injected colored solution confined by liquid pinning. Scale bar: 6 mm. **(G)** A master mold of the μMeRe device fabricated with desktop micromilling that accommodates different device designs. **(H)** Devices can be deployed as a culture platform on commercial cell culture plates for enhanced scalability. Scale bar: 3 mm.

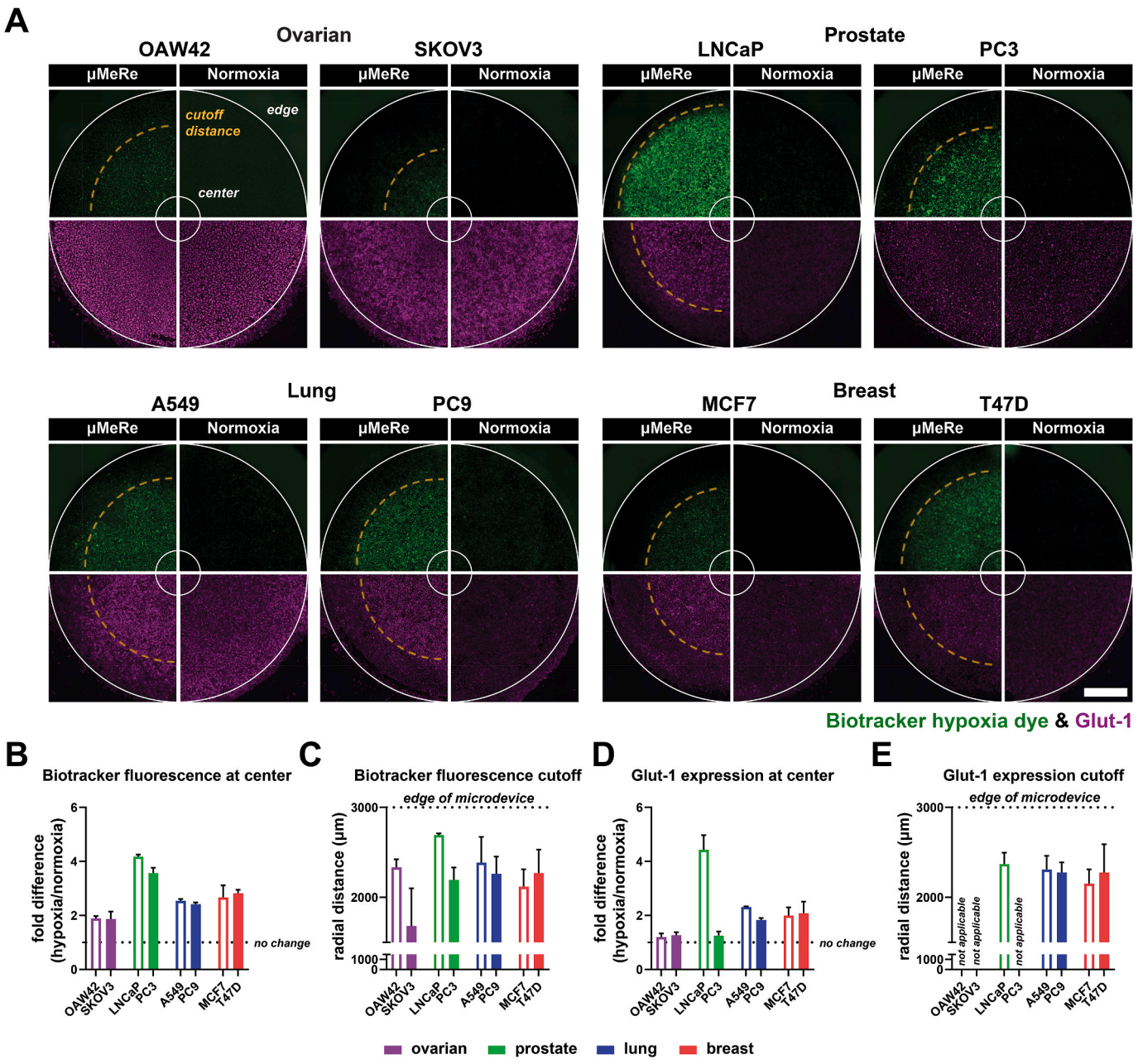

Fig. 2. Intertumoral heterogeneity in the expression of hypoxia and glycolysis markers is revealed by the μMeRe assay. **(A)** Hypoxia landscapes in μMeRe and normoxia devices. Green: BioTracker™ hypoxia dye staining; purple: Glut-1 immunostaining. Dashed lines: radial cutoff distance of fluorescence signal (defined as a 30% drop from the peak value at the center). Scale bar: 1000 μm. **(B)** Fold differences in BioTracker hypoxia dye fluorescence intensity at the center of the μMeRe vs. the normoxia devices for each cancer cell line. **(C)** Radial cutoff distances of the BioTracker hypoxia dye fluorescence signals in the μMeRe device for each cancer cell line. **(D)** Fold differences in Glut-1 fluorescence intensity at the center of the μMeRe vs. the normoxia devices for each cancer cell line. **(E)** Radial cutoff distances of Glut-1 fluorescence in the μMeRe device for each cancer cell line. **(B–E)** Error bars: standard deviation, $n = 6$ for each condition.

3000 μm, we can calculate the percentage of hypoxic or rewired cells within the μMeRe devices using the cutoff distance. For instance, ~80.5% of the LNCaP prostate cancer cells and ~31.4% of the SKOV3 ovarian cancer cells were hypoxic. On the other hand, the LNCaP prostate cancer cells also showed the highest increase (>4.4-fold) and the greatest cutoff distance (~2370 μm; or ~62.4% of micropattern area) in Glut-1 expression (Fig. 2D and E). Surprisingly, Glut-1 upregulation over normoxia control was not seen in the two ovarian cancer cells, OAW42 and SKOV3, nor in the PC3 prostate cancer cells in the μMeRe devices (Fig. 2D). As a result, they did not have a cutoff distance in Glut-1 staining (Fig. 2E). Overall, the LNCaP prostate cancer cells generated the most hypoxic TME and had the greatest metabolic rewiring indicated by Glut-1, while the SKOV3 ovarian cancer cells created the least hypoxic TME without discernible changes in Glut-1 expression. Notably, compared to the prominent differences observed in the μMeRe assay, the differences in the metabolic rewiring behaviors of LNCaP cells and SKOV3 cells could not be easily observed using a hypoxia incubator (Fig. S1). The μMeRe assay thus reveals a high level of heterogeneity in the capabilities of different cancer cells in driving a hypoxic TME and undergoing metabolic rewiring.

2.3. μMeRe assay reveals intertumoral heterogeneity in metabolism-related gene expression

To further resolve the observed heterogeneity in rewiring behaviors, we examined the differential gene expression of cancer cells cultured in the μMeRe device over their normoxia control (Fig. 3A). All devices were disassembled after 24 h of culture to extract cancer cells from the whole micropattern for RNA isolation and reverse transcription-quantitative polymerase chain reaction (RT-qPCR). The panel consists of 13 genes related to cellular metabolism, including glycolysis, OXPHOS, and mitochondrial electron transport chain (ETC). We observed metabolic rewiring from OXPHOS to glycolysis in all the cancer types, as glycolysis-associated genes were upregulated and those related to OXPHOS and mitochondrial ETC were downregulated (Fig. 3B). A closer examination reveals a cancer cell line-specific difference in the magnitude of gene expression changes induced by the μMeRe device (over the normoxia counterpart). Notably, hexokinase 2 (HK2) was highly upregulated in A549 and PC9 lung cancer cells (~4.4 and ~2.9 in $\log_2$(fold change), respectively) and OAW42 ovarian cancer cells (~3.1 in $\log_2$(fold change)). Interestingly, SKOV3 ovarian cancer cells and PC3 prostate cancer cells had minimal upregulation of glycolysis-related genes (~0.5 and ~0.3 in $\log_2$(fold change), respectively). SKOV3 ovarian cancer cells also showed the least downregulation of gene expression related to OXPHOS and mitochondrial ETC (~−0.3 and ~ −0.5 in $\log_2$(fold change), respectively). In contrast, LNCaP prostate cancer cells had the greatest downregulation of OXPHOS and mitochondrial ETC (~−1.4 and ~ −1.5 in $\log_2$(fold change), respectively) (Fig. 3B). Overall, when measured by the average of absolute $\log_2$(fold) values in the 13-gene panel, LNCaP prostate cancer cells had the highest and SKOV3 ovarian cancer cells had the least gene expression changes in the μMeRe device, which is consistent with the finding from BioTracker hypoxia dye and Glut-1 staining (Fig. 2).

To examine the relationship between imaging- and gene expression-based metabolic rewiring activities, we next developed an aggregated metric, MeRe (Metabolic Rewiring) score, from both analyses for each examined cancer cell line (see Methods) (Table S1). Briefly, imaging-based MeRe scores were constructed using the fold change of fluorescence intensity at the center of the μMeRe device over their normoxia counterparts and the radial distance of the fluorescence signal observed in the μMeRe device (from the center to the point where the fluorescence intensity falls below 70% of the measured intensity at the center). Gene expression-based MeRe scores were constructed using the $\log_2$(fold change) of the metabolism-related genes and multiplying the expression change with a weight score, either −1 (genes related to OXPHOS or mitochondrial ETC) or 1 (genes related to glycolysis), to indicate the metabolic shift from OXPHOS to glycolysis. Overall, the image-based scores reflect the changes in hypoxia/glycolysis markers (i.e., phenotype/protein expression), while the gene expression-based scores reflect the changes in the mRNA levels of metabolism-related genes.

We found a weak correlation ($R^2 = 0.32$, $p = 0.14$), between the imaging- and gene expression-based scores (Fig. 3C). The correlation between the two scores (albeit weak) demonstrated an overlap between the changes measured through the two approaches. Additionally, the weak correlation also indicated that the two scores contained distinct information on the heterogeneity of the metabolic rewiring behaviors in different cancer cell lines. A closer examination revealed that several cancer cell lines demonstrated differences between hypoxia/glycolysis marker expression and gene expression. For instance, the PC9 and A549

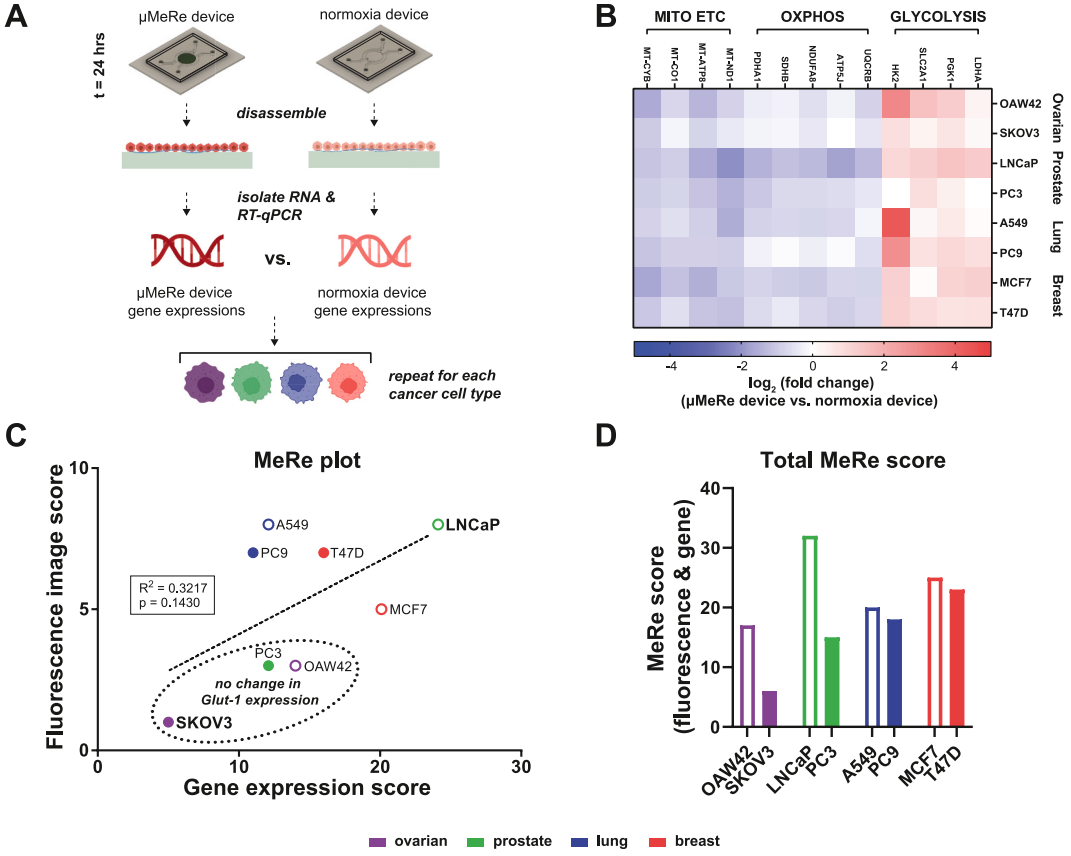

Fig. 3. μMeRe assay reveals intertumoral heterogeneity in metabolism-related gene expression. **(A)** A schematic of the RNA isolation workflow. Differential gene expression analysis was performed between cells extracted from the μMeRe device vs. the normoxia counterpart for each cell line. **(B)** A heatmap of the metabolism-related differential gene expression. Mito ETC: mitochondrial electron transport chain. OXPHOS: oxidative phosphorylation. RNA samples were obtained from $n = 3$ per condition. **(C)** Distribution of the cancer cell panel based on the fluorescence image-based (y-axis) vs. gene expression-based (x-axis) MeRe scores. Pearson correlation analysis was performed between the two scores. **(D)** Total MeRe scores of the cancer cell panel.

lung cancer cells showed high upregulation of hypoxia/glycolysis markers (i.e., high fluorescence image-based MeRe scores), but their gene expression-based MeRe scores were similar to those of OAW42 ovarian cancer cells and PC3 prostate cancer cells, which did not show an increase in Glut-1 expression in the μMeRe device over their normoxia control.

Since the two scores provide distinct insights into the metabolic rewiring behavior, they were combined into a total MeRe score to describe the overall metabolic rewiring behavior for each cancer cell line (Fig. 3D). When we combined the fluorescence image- and gene expression-based scores into the total MeRe scores, we observed similar levels of metabolic rewiring behaviors in the two lung cancer cells, A549 and PC9, as well as the two breast cancer cells, MCF7 and T47D. Through both the MeRe plot (Fig. 3C) and the total MeRe scores (Fig. 3D), we also identified cancer cell lines with the most distinct rewiring behaviors. The LNCaP prostate cancer cells and the SKOV3 ovarian cancer cells were at opposite ends of the MeRe plot, with the highest and the lowest total MeRe scores, respectively (Fig. 3C and D). Overall, the MeRe score indicates the magnitude of metabolic rewiring toward a more glycolytic, less OXPHOS phenotype within μMeRe devices (over their normoxia counterparts), which reflects the cancer cell's capability to: **1)** establish a hypoxic TME, and **2)** undergo metabolic rewiring in response to the newly established hypoxic microenvironment.

2.4. RNA-seq confirms heterogeneity and commonality of rewiring behaviors in μMeRe assay

Our MeRe scores have been established with a selected set of exogenous and endogenous hypoxia markers and a panel of metabolism-related genes. We next cross-checked our MeRe scores with transcriptomic analysis using RNA sequencing (RNA-seq). All μMeRe and corresponding normoxia devices were disassembled after 24 h of culture to expose the micropatterns for cancer cell extraction, RNA isolation, and RNA-seq. The transcriptomic profiles of all 8 cancer cell lines in the μMeRe and normoxia devices were analyzed (Fig. 4A). Notably, the differences between cancer cell lines were significantly more pronounced than the differences between μMeRe and normoxia devices for the same cancer cell lines (Fig. 4A and B). To identify differentially expressed genes (DEGs) in the oxygen-limited microenvironment, transcriptome-wide pairwise gene expression analysis was performed between the μMeRe device and its normoxia counterpart for each cancer cell line (Fig. 4C). DEGs were selected based on the criteria of absolute $\log_2$(fold change) of no less than 2 (i.e., $|\log_2(\text{fold change})| \geq 2$) and the false discovery rate (FDR) of less than 0.05 (i.e., FDR <0.05). Interestingly, the number of DEGs were similar in cancer cells from the same organ of origin (except the two ovarian cancer cell lines). The prostate (LNCaP and PC3) and lung (A549 and PC9) cancer cells had a greater number of DEGs compared to the breast (MCF7 and T47D) and ovarian (OAW42 and SKOV3) cancer cells. Coincidental to their MeRe scores, LNCaP prostate cancer cells showed the greatest number of DEGs (368 DEGs), whereas SKOV3 ovarian cancer cells had the lowest number of DEGs (49 DEGs).

To visualize the shared and the distinct DEGs across different cancer cell lines, we next organized the 8 sets of DEGs in an UpSet plot [29] (Fig. 4C). The intersections of cancer cell line-specific DEGs are plotted as a matrix (under the x-axis), where the colored individual circles denote the unique DEGs in specific cancer cell lines and the line-connected black or orange circles indicate the intersections (i.e., the unique DEGs shared by the specified pairs or groups of cell lines). The corresponding bar graph above the colored circles shows the number of (shared) unique DEGs. Notably, LNCaP prostate cancer cells showed the greatest number of distinct DEGs across all cancer types, where 231 out of its 368 DEGs were unique to LNCaP prostate cancer cells. In contrast, SKOV3 ovarian cancer cells only had 13 out of its 49 DEGs that were unique. Furthermore, we identified 5 DEGs that were shared across all the cell lines, which include genes related to glycolysis and lipoprotein metabolism (*ALDOC, ANGPTL4, HK2*), hypoxia (*NDRG1*), and apoptosis (*BNIP3*).

We investigated the clinical significance of the five genes using patient data from The Cancer Genome Atlas (TCGA) database [30]. We performed pooled survival analysis to evaluate the association between the expression levels of each identified gene and patient survival outcomes (Fig. 4D). In alignment with the cancer types examined in the μMeRe assay, patient samples ($n = 2950$) of ovarian (OV), prostate (PRAD), lung (LUAD and LUSC), and breast (BRCA) cancer were combined. The patient cohorts were then stratified into high (top 25%), and low (bottom 25%) expression groups based on the expression levels of each gene, and survival curves were generated for each group to assess differences in survival. Impressively, with the exception of *HK2*, the remaining four genes exhibited a highly significant positive hazard ratio (HR) in the selected cancer types, indicating a strong association between higher expression levels and poorer patient survival outcomes. Next, we recognized that the five genes identified by the μMeRe assay were not collectively found in the established hypoxia gene signatures [31]. This led us to ask whether their expression levels correlate with hypoxia-associated genes in patient samples. A hypoxia gene signature was defined by selecting a set of 7 genes (*VEGFA, ADM, LDHA, P4HA1, SLC2A1, PGK1, DDIT4*) commonly reported in the literature [32–34]. We performed Pearson correlation analyses to assess the relationship between the average expression levels of the 5 identified genes and those of the 7 hypoxia genes in patient samples of ovarian, prostate, lung, and breast cancer (Fig. S2). A strong correlation was observed between the expression levels of the two gene sets, indicating that the identified genes are likely associated with hypoxia-related pathways despite not being part of the traditional hypoxia gene signatures.

Next, we performed pathway enrichment analysis using Partek Flow on the selected DEGs of each cancer type, which identifies involved biological pathways with their respective enrichment scores. We focused on the HIF-1 signaling pathway and glycolysis in all the analyzed cancer cells and compared the enrichment scores to their corresponding total MeRe scores (Fig. 4E and F). Notably, the MeRe scores showed a significant correlation ($R^2 = 0.64$, $p = 0.02$) with the enrichment scores of the HIF-1 signaling pathway (Fig. 4F). In contrast, they are only weakly correlated ($R^2 = 0.32$, $p = 0.15$) with those of glycolysis (Fig. 4H). We further performed a comprehensive pathway enrichment analysis using Ingenuity Pathway Analysis (IPA) to identify the top canonical pathways based on the activation Z-score (i.e., a quantity that determines whether a biological function has significantly more "increased" predictions than "decreased" predictions [35]) and -$\log_{10}$(P value) (Tables S2 and 3). From this list, 10 relevant canonical pathways with the highest activation Z-score (Fig. 4I) and -$\log_{10}$(P value) (Fig. 4J) were selected. Under both analyses, we observed that glycolysis, gluconeogenesis, and HIF-1α signaling were commonly enriched in all cancer types, with LNCaP prostate cancer cells showing the highest enrichment of glycolysis and SKOV3 ovarian cancer cells showing the lowest. Our RNA-seq data thus confirmed the heterogeneity and commonality of rewiring behaviors observed in the imaging- and qPCR-based μMeRe assay.

2.5. Biosensor reveals differential oxygen sensitivity in HIF-1 response for cells with distinct MeRe scores

Considering the strong correlation between the MeRe score and the HIF-1α pathway (Fig. 4E), we next assessed the HIF-1α signaling activity in cancer cells within the μMeRe device. HIF-1α degrades rapidly (<5 min) under normoxic conditions, making it difficult to capture the HIF-1 activity through immunostaining [36]. Therefore, a HIF-1-dependent reporter gene was introduced into the cancer cells to monitor the HIF-1 activity. The reporter was modified from a construct developed by Erapaneedi et al. [37]. It consists of a hypoxia-sensing promoter region with 5 × hypoxia-responsive element (HRE), a reporter region with a fluorescent protein UnaG fused with a PEST degron sequence motif (to

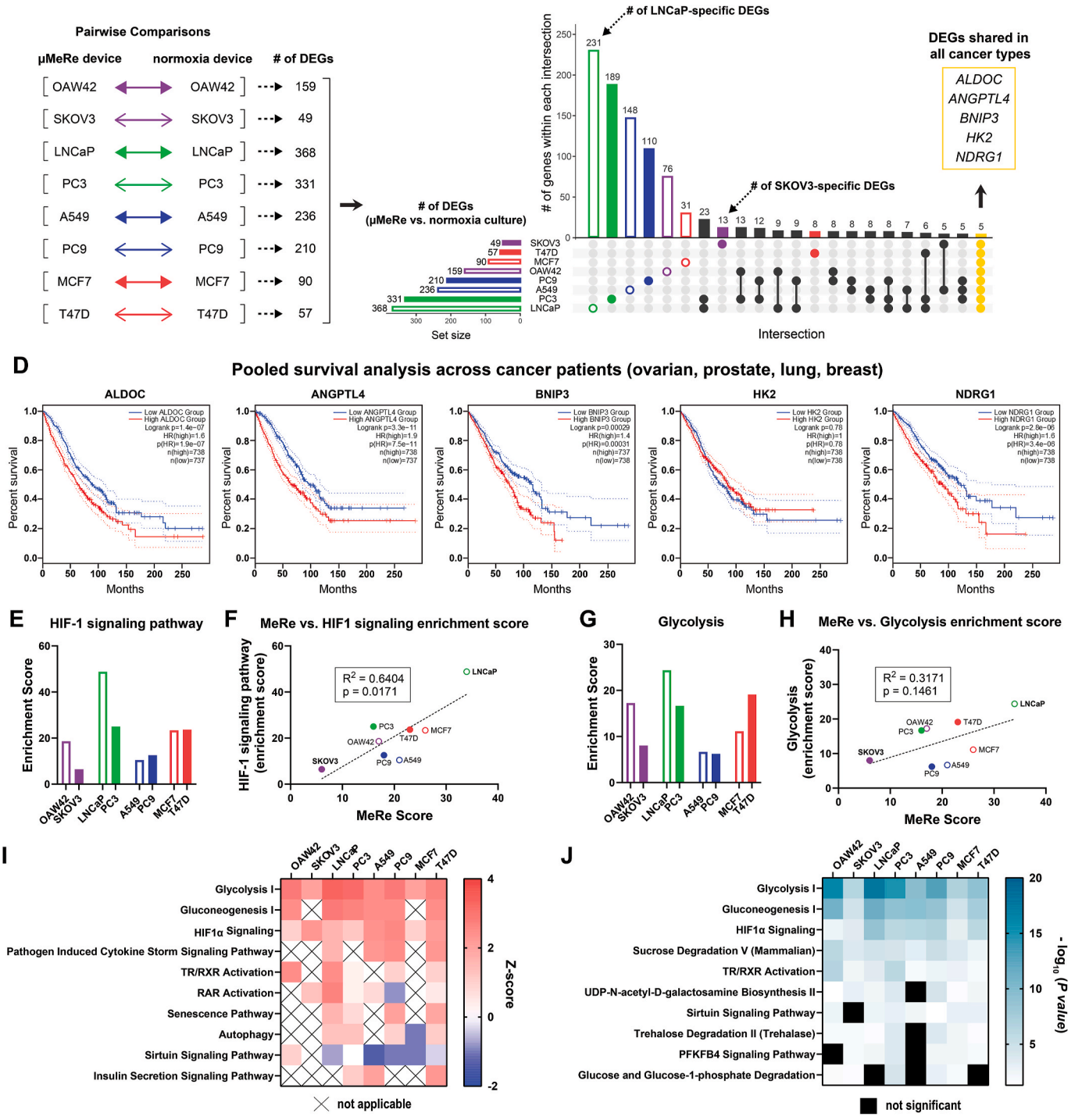

Fig. 4. RNA-seq confirms heterogeneity and commonality of rewiring behaviors in μMeRe assay. **(A)** Hierarchical clustering heatmap of gene expression for the 8 cancer cell lines cultured in μMeRe and normoxia devices. $N = 2$ per condition for bulk RNA-seq. **(B)** A 3-D PCA plot of the 8 cancer cell lines from μMeRe and normoxia devices based on the bulk RNA-seq data. **(C)** An UpSet plot of differentially expressed genes (DEGs; individual and shared in all the examined cancer cell lines). DEGs were identified and selected from those meeting the criteria of $|\log_2(\text{fold change})| \geq 2$ and FDR <0.05 in the μMeRe device over the normoxia control. **(D)** Kaplan-Meier survival curves for pooled patients ($n = 2950$) of ovarian cancer (OV), prostate cancer (PRAD), lung cancer (LUAD and LUSC), and breast cancer (BRCA) when tumors are partitioned into high (top 25%) and low (bottom 25%) quantiles based on the expression levels of the indicated gene. Dotted lines indicate a 95% confidence interval. The hazard ratio (HR) and P value were calculated based on the Cox Proportional-Hazards (PH) Model. **(E to H)** Enrichment scores from pathway enrichment analysis and their correlations with the MeRe scores. Pearson correlation analysis was performed between the scores. **(E, F)** HIF-1 signaling pathway. **(G, H)** Glycolytic pathway. **(I to J)** Heatmaps of selected canonical pathways based on the **(I)** Z-score and **(J)** $-\log_{10}(P \text{ value})$ across the cancer cell panel in the μMeRe device.

enhance UnaG turnover), and a truncated CD19 (tCD19) under a constitutive PGK promoter for cell sorting (Fig. 5A). The hypoxia biosensor facilitates the monitoring of the dynamic HIF-1 activity in real-time without the need for device disassembly or staining.

We chose LNCaP prostate cancer cells and SKOV3 ovarian cancer cells for the biosensor-based analysis of HIF-1 activity, as they occupy the two ends of the MeRe spectrum and have consistently shown distinct rewiring behaviors within the μMeRe device. Both cancer cell lines were transduced with the biosensor construct and sorted based on the constitutive tCD19 marker expression (Fig. S3). The sorted LNCaP UnaG tCD19 and SKOV3 UnaG tCD19 cells were cultured in μMeRe devices for 24 h before imaging, and the HIF-1 activity of each cancer cell line was measured through the UnaG fluorescence intensity. Consistent with the findings from BioTracker hypoxia dye and Glut-1 staining, LNCaP and SKOV3 cells showed distinct HIF-1 activity in the μMeRe device (Fig. 5B). LNCaP cells showed significantly higher UnaG expression than SKOV3 cells at the center and intermediate regions of the μMeRe device (Fig. 5C). Interestingly, SKOV3 cells also showed an upregulation of UnaG signal at the center over the periphery in the μMeRe device, although it was not as pronounced as that of LNCaP cells.

This led us to ask whether the observed differences in the HIF-1 activities were due to the differences in their responsiveness to the oxygen landscape. To address this question, we cultured the biosensor-transduced LNCaP and SKOV3 cell lines in the normoxia devices in an oxygen-controlled incubator, which allows for equilibration of the oxygen levels in the device to those of the incubator (Fig. 5D). For each condition, the oxygen level was chosen from a series ranging from normoxia to severe hypoxia (21%, 4%, 2%, and 1% O_2). At the end of 24 h of incubation, we examined their UnaG expression as a function of oxygen concentration using live fluorescence microscopy (Fig. 5E–G). LNCaP cells showed higher UnaG expression in 1% O_2 (Fig. 5E), while SKOV3 cells had limited increase in UnaG expression below 2% O_2 (Fig. 5F). Interestingly, UnaG expression at 4% O_2 was only observed in SKOV3 cells, which suggests that SKOV3 cells have a higher intrinsic oxygen threshold (i.e., oxygen level that triggers its HIF-1 activity) compared to LNCaP cells. The oxygen threshold was calculated to be ~2.2% O_2 for LNCaP cells and ~3.7% O_2 for SKOV3 cells, which were obtained by interpolating the oxygen concentration that resulted in 50% of the maximum measured UnaG fluorescence (i.e., at 1% O_2) (Fig. 5G). Our data suggest that distinct characteristics of HIF responses, e.g., the oxygen threshold to trigger HIF activities and the magnitude of HIF responses, may underlie the observed differences in the metabolic rewiring behaviors of cancer cells in the μMeRe devices.

Given the distinct HIF-initiating oxygen thresholds observed in the two cell lines, we investigated the potential mechanism behind their differing oxygen-sensing capabilities. Mitochondria have been recognized as the major metabolic and signaling hub for cellular oxygen sensing and HIF-1 activation [38,39]. Studies suggest that mitochondria regulate hypoxia-induced responses through complex III in the mitochondrial ETC, which generates mitochondrial reactive oxygen species (ROS) that serve as hypoxia signaling molecules [40,41]. We thus examined whether LNCaP and SKOV3 cells show differential ROS production in response to hypoxia. Two methods of hypoxia-induction were utilized for the study: μMeRe device in the standard incubator and normoxia device in the 1% O_2 incubator (Fig. 5H). ROS production of each cancer cell line was measured with CM-H_2DCFDA (a fluorescent dye-based indicator of ROS). After 24 h of culture, a significant increase in ROS signal was only observed in LNCaP cells at the center of the μMeRe device, which was absent in SKOV3 cells (Fig. 5I and J). Consistent with the findings from the μMeRe device-cultured cells, a significant increase in ROS signal was only observed in LNCaP cells in normoxia device under 1% O_2 (Fig. 5K and L). Overall, our results suggest that the differing hypoxia-induced rewiring behaviors of the identified distinct cancer types may have originated from the mitochondria through ROS regulation.

2.6. Targeting oxidative metabolism alleviates hypoxia-induced therapy resistance

Hypoxia can induce molecular and cellular changes in cancer cells that promote chemotherapeutic resistance, such as upregulating the expression of drug resistance genes and drug efflux proteins [20]. Therefore, alleviating the severity of hypoxia in the TME may restore chemotherapeutic efficacy. Cancer treatment by cisplatin, a widely used first-line treatment, often results in limited response and a high rate of recurrence, which has been largely attributed to the hypoxia-induced therapy resistance [42,43]. A promising countermeasure is to reduce the severity of hypoxia by inhibiting mitochondrial activity (Fig. 6A). Atovaquone (ATO), an FDA-approved anti-malarial drug, can decrease cellular oxygen consumption rate (OCR) by inhibiting mitochondrial omplex III and has been shown to decrease hypoxic gene expression in lung cancer patients [44,45]. Therefore, we examined whether ATO can alleviate hypoxia-induced metabolic rewiring as well as cisplatin resistance in μMeRe devices using cancer cells with distinct metabolic rewiring behaviors.

LNCaP and SKOV3 cells were cultured in the μMeRe device for 12 h before being treated with 40 μM atovaquone for another 12 h. Cells were then characterized for their radial profiles of hypoxic states by BioTracker hypoxia dye staining, followed by Glut-1 immunostaining (Fig. 6B–E). For LNCaP cells, ATO treatment eliminated the elevated BioTracker hypoxia dye signal seen in the untreated control, while the radial cutoff distance for the increased Glut-1 expression decreased by ~245 μm (Fig. 6B and C). For SKOV3 cells, atovaquone treatment also abolished the enhanced BioTracker hypoxia dye signal. However, changes in the radial profiles of Glut-1 expression were minimal (Fig. 6D and E). Our results indicate that mitochondrial inhibition is effective in reducing the severity of hypoxia in both cancer types, as well as the magnitude of phenotypic change in the hypoxia-responsive LNCaP cells.

We further examined the changes in gene expression upon ATO treatment, using RT-qPCR and the gene panel from Fig. 3B. The gene expression profiles in the untreated (control) and ATO-treated μMeRe devices were measured as $\log_2$(fold change) from the untreated counterparts in normoxia devices (Fig. 6F). For LNCaP cells, ATO treatment reduced the downregulation of OXPHOS- and mitochondrial ETC-related genes, to the levels similar to those in the untreated normoxia device. Interestingly, we observed a mixed trend in glycolysis-related genes, where *SLC2A1* was downregulated, while the rest were upregulated in the ATO-treated condition. In contrast, for SKOV3 cells, ATO treatment slightly reduced the upregulation of glycolysis-related genes and the downregulation of mitochondrial ETC, while inducing a more notable downregulation of OXPHOS-related genes in μMeRe devices (Fig. 6F). As such, similar to the phenotypic changes, mitochondrial inhibition also had a more pronounced effect on reducing the gene expression changes in the hypoxia-responsive LNCaP cells.

Next, we evaluated whether reducing the severity of hypoxia and hypoxia-induced rewiring can improve cisplatin response. LNCaP and SKOV3 cells were cultured in the μMeRe and normoxia devices for 12 h before being treated with 40 μM ATO for 12 h, followed by a combined treatment of 40 μM ATO and 500 μM cisplatin for an additional 24 h. The combination therapy was compared to the cisplatin-alone control, where cells were incubated in the μMeRe and normoxia devices for 24 h followed by 500 μM cisplatin treatment alone for another 24 h. The therapy response was evaluated through the radial profiles of live cell fractions (measured by the local areal density of live cells, see Methods) in the cancer micropatterns after treatment. We observed hypoxia-induced cisplatin resistance in LNCaP cells, as those cultured in the μMeRe device exhibited a higher live areal density compared to their normoxia counterpart following cisplatin treatment (Fig. 6G–I). Combining ATO and cisplatin effectively lowered the LNCaP cell viability near the edge of the μMeRe device (>2100 μm from the center), where the live fraction decreased from ~50% to ~25% (Fig. 6I). For SKOV3 cells, we did not observe hypoxia-induced cisplatin resistance in

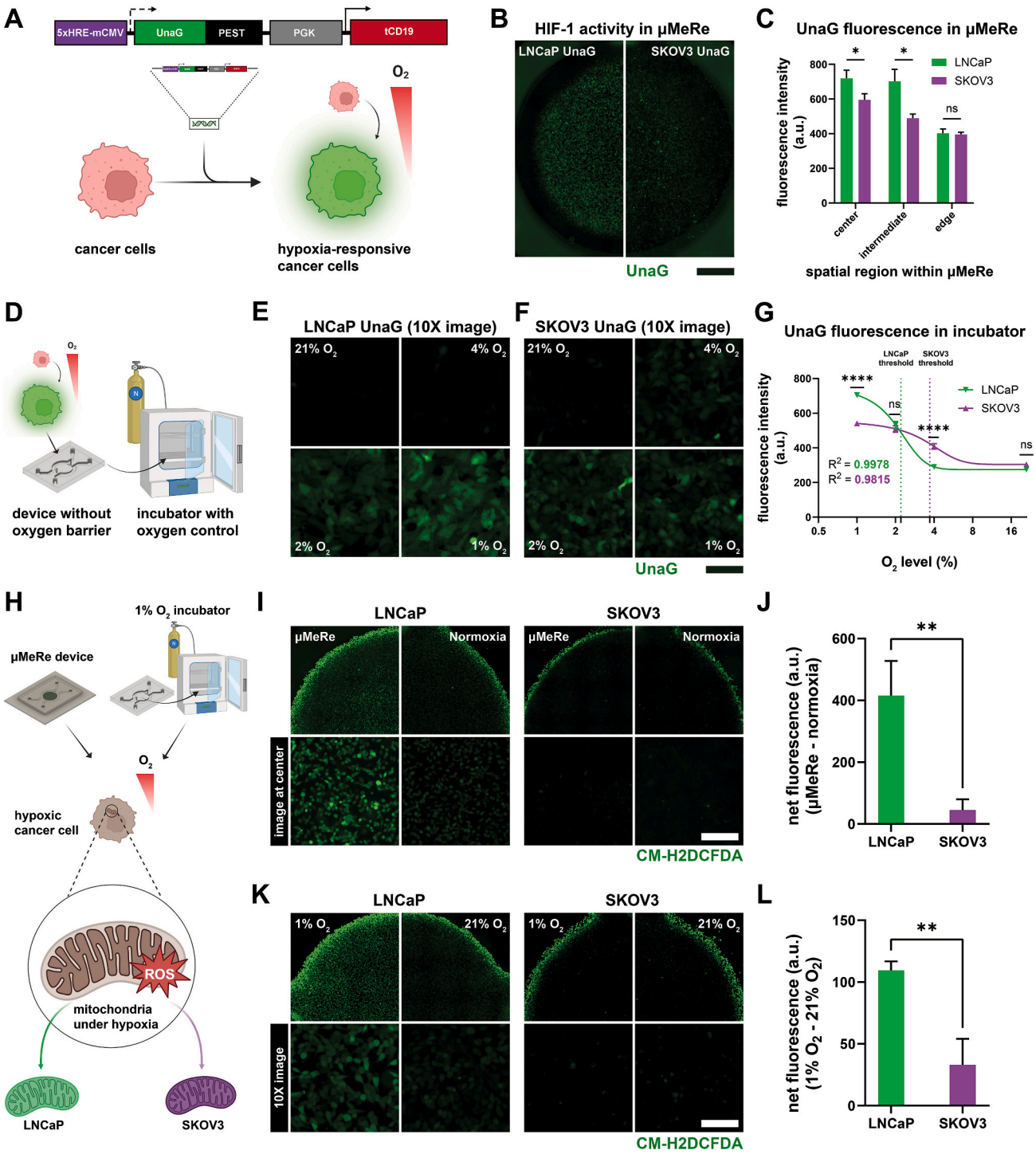

Fig. 5. Distinct oxygen sensitivity for HIF-1 activation and mitochondrial ROS signaling in LNCaP and SKOV3 cells. **(A)** A schematic of the biosensor construct for live monitoring of HIF-1 signaling activities. **(B)** Hypoxia biosensor-transduced cancer cells cultured in the μMeRe device and their response in UnaG expression (green). Scale bar: 1000 μm. **(C)** Quantification of UnaG fluorescence intensity measured at different spatial regions in the μMeRe device for the two cancer cell lines. *P < 0.05 by Student's t-test. **(D)** The workflow of biosensor-transduced cancer cell culture in an oxygen-controlled incubator. UnaG expression in **(E)** LNCaP cells and **(F)** SKOV3 cells after 24 h of culture under different oxygen levels (21%, 4%, 2%, and 1% O_2). Green: UnaG. Scale bar: 100 μm. **(G)** UnaG fluorescence intensities vs. oxygen levels for LNCaP and SKOV3 cells and respective curve fitting. ****P < 0.0001 by two-way ANOVA followed by Šídák's multiple comparisons test (comparing mean fluorescence intensities between the two cell lines at each oxygen level). ns, not significant. **(H)** A schematic of measuring mitochondrial reactive oxygen species (ROS) production. **(I)** ROS levels in LNCaP (left) and SKOV3 (right) cells in the μMeRe and normoxia microdevices measured by CM-H_2DCFDA (green). **(J)** The net fluorescence intensity of ROS staining for each cancer cell line (measured as the difference at the center of the μMeRe device vs. the normoxia control device). **(K)** ROS staining (green) in LNCaP (left) and SKOV3 (right) cells under 1% O_2 and 21% O_2. **(L)** Change in the fluorescence intensity of ROS staining for each cancer cell line in 1% O_2 vs. 21% O_2. **(I, K)** Scale bar: 1000 μm (top panels) and 100 μm (bottom panels). **(J, L)** **P<0.01 by Student's t-test. All error bars: standard deviation from $n = 6$.

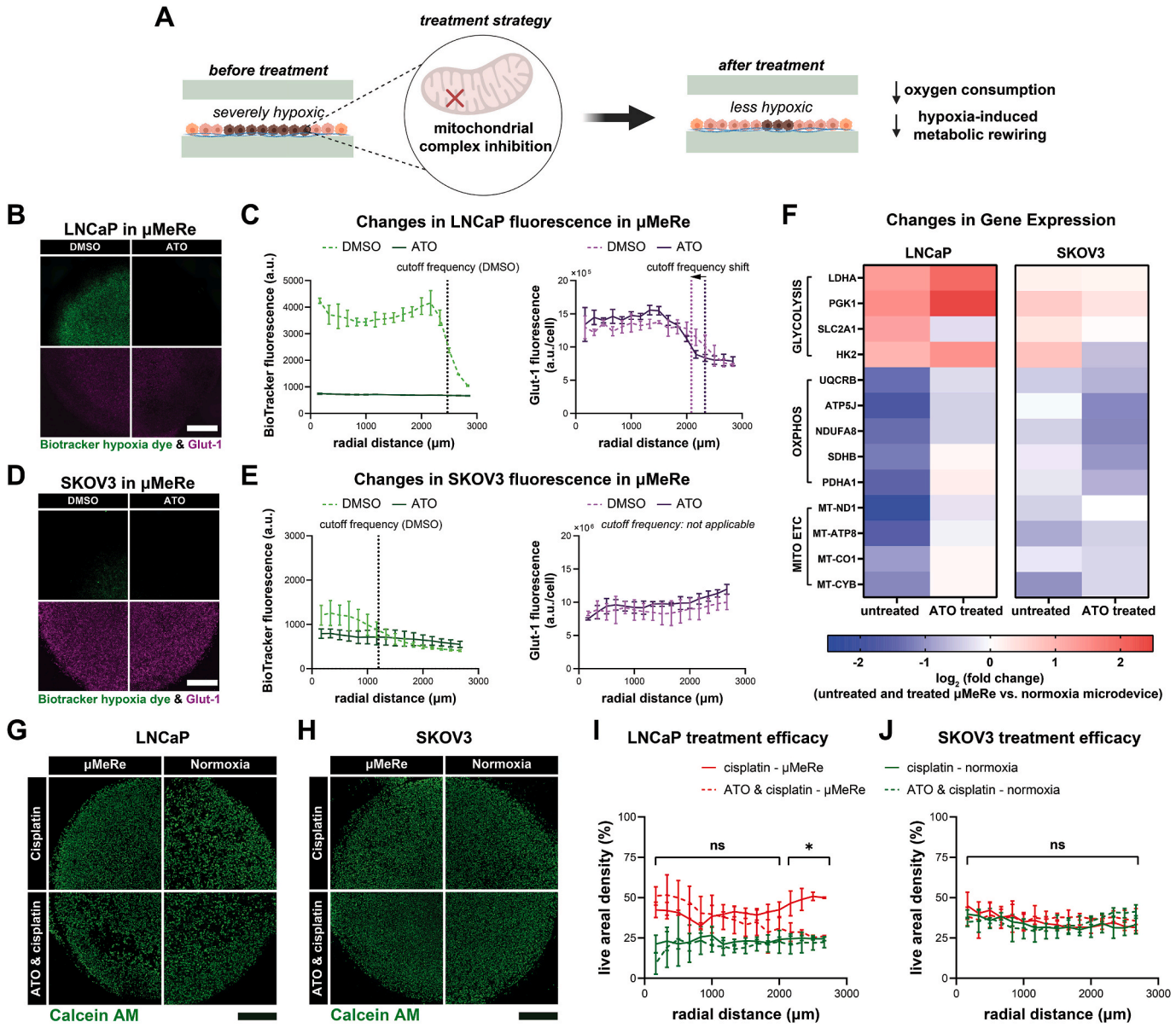

Fig. 6. Inhibiting mitochondrial complex alleviates hypoxia-induced therapy resistance. **(A)** A schematic of the treatment strategy targeting the mitochondrial complex in the hypoxic tumor microenvironment. **(B** to **E)** The treatment effect of atovaquone (ATO), a mitochondrial complex inhibitor, on the expression of hypoxia markers in **(B)** LNCaP and **(D)** SKOV3 cells in the μMeRe device. Changes in the radial profiles of BioTracker hypoxia dye staining (left, green lines) and Glut-1 immunostaining (right, purple lines) in **(C)** LNCaP and **(E)** SKOV3 cells in the μMeRe devices with and without ATO treatment. **(F)** Changes in the relative expression of metabolism-related genes in μMeRe vs. normoxia device without or with ATO treatment. RNA samples were obtained from $n = 3$ per condition. **(G** to **J)** Efficacy of cisplatin and ATO/cisplatin combination therapy on **(G)** LNCaP and **(H)** SKOV3 cells in μMeRe and normoxia devices. Viability of the **(I)** LNCaP and **(J)** SKOV3 cells is measured as the radial profiles of the live cell areal density for each treatment condition. Statistical significance (*$P < 0.05$) was determined by two-way ANOVA followed by Šídák's multiple comparisons test. In the figure, only the comparison between cisplatin–μMeRe and ATO & cisplatin–μMeRe at the indicated radial distance is highlighted. **(B, D, G, H)** Scale bar: 1000 μm. All error bars: standard deviation from $n = 6$. ns: not significant.

the μMeRe device, or any synergistic benefits of ATO and cisplatin combination (Fig. 6H–J). Overall, our results indicate that the benefits of mitochondrial inhibition are more pronounced against hypoxia-responsive cancer types.

3. Discussion

Here, we developed a micro-metabolic rewiring (μMeRe) assay to measure the ability of cancer cells to drive hypoxia and subsequent metabolic rewiring in an oxygen-limited microenvironment. The device was fabricated with micro-milling, which was much more cost-effective than the conventional photolithography-based microfabrication methods. The cellular metabolism-driven hypoxia induction mirrors the in vivo mechanism of hypoxia formation [46]. This allows hypoxia to be induced in the device in a standard incubator without needing any external oxygen control or complex tubing [47,48]. These features enhance the simplicity and scalability of our assay for basic research and preclinical therapeutic tests or screenings.

In addition to hypoxia, studies have also highlighted other factors that can shift tumor metabolism, including intrinsic (e.g., altered genes) and extrinsic cues (e.g., nutrient availability) [49]. Notably, the physical barriers in our devices also impose a diffusion limit on nutrients and other soluble factors, which will generate concentration gradients across the radius of the tumor micropattern like those in real tumors. In this

context, we can incorporate other factors in our assay (e.g., glucose and glutamine availability), for example, by modulating the concentration of glucose and other metabolic amino acids in our cell culture media (e.g., high vs. low concentration) and/or comparing them between μMeRe vs. normoxia devices. Additionally, hypoxia-induced acidosis and its impact on tumor responses to chemotherapies may be investigated by employing bicarbonate-free cell culture media and measuring pH changes in our devices. Furthermore, our μMeRe device can easily incorporate other components of the TME, such as stromal cells (e.g., cancer-associated fibroblasts) and ECM (e.g., collagen), to enhance the physiological relevance of the established TME. Notably, cancer-associated fibroblasts can actively contribute to metabolic rewiring by releasing lactate, which is then taken up by tumor cells to generate NADH for ATP, ultimately fueling tumor growth [50]. The modularity of our assay can be leveraged to further investigate how the different components influence the rewiring behavior of cancer cells.

Current methods of characterizing cancer metabolism include metabolomics, extracellular flux analysis, single-cell metabolic analysis, and functional genomic screening [51]. These strategies each provide unique insights into the metabolic status of tumor tissue. Notably, extracellular flux analysis (e.g., Agilent Seahorse XF analyzer) is one of the most common and simple methods for characterizing the bioenergetic activity of live cells, including measuring the OCR and the extracellular acidification rate (ECAR) of cultured cells. However, the influence of the TME, including hypoxia, is often omitted in these measurements. Alternatively, various cutting-edge techniques, such as single-cell energetic metabolism by profiling translation inhibition (SCENITH) and single-cell RNA-sequencing (scRNAseq), provide a snapshot of tumor tissue metabolism at the single-cell resolution [52,53]. However, the high cost and specialized equipment associated with these techniques make them more suitable for the later stages of preclinical studies. Furthermore, it is difficult to assess the influence of hypoxia from the obtained "snapshots" since the hypoxia landscape of the original TME is disrupted during sample preparation for flow cytometry, which is conducted in well-oxygenated conditions. The metabolic analyses in our μMeRe assay are performed without disrupting the established hypoxia landscape, providing a unique insight into the interplay between hypoxia and metabolic rewiring that is not easily obtained using existing methods. Our assay may integrate with imaging-based mass spectrometry techniques, such as matrix-assisted laser desorption/ionization-mass spectrometry imaging (MALDI-MSI), to measure glycolytic and mitochondrial metabolites and visualize metabolic rewiring behaviors in a spatially resolved manner.

Although all cancer cell lines used in the study established hypoxia in the μMeRe device, we observed vast differences in the severity and the radial profiles of their hypoxic landscapes, where LNCaP and SKOV3 cells established the most and the least hypoxic TME, respectively. As the severity of hypoxia is determined by oxygen consumption in the model, our results suggest a high level of heterogeneity in oxygen demand between different cancer cells. This aspect is often omitted in studies where hypoxia is “forced” onto cancer cells by a hypoxia incubator under a predetermined oxygen level [25,54,55]. Furthermore, studies have shown that cells orchestrate hypoxia-mediated adaptation responses that vary depending on the duration of hypoxia (e.g., acute, chronic, and cyclic) [56,57]. For instance, the protein levels of HIF-1α in A549 lung cancer cells peaked at 4 h of exposure to severe hypoxia (0.5% O_2), but decreased with sustained hypoxia exposure [58]. Therefore, our assay may further resolve the heterogeneity of cancer cells by extending the culture duration to observe differences in their response to prolonged hypoxia.

Recreating metabolism-driven hypoxic TME allows for observing cell-specific metabolic rewiring behaviors. Glut-1 expression was measured to indicate metabolic changes toward glycolysis in the μMeRe assay. Glut-1 mediates the influx of glucose for glycolysis and is upregulated as a compensatory response when OXPHOS is disrupted [59,60]. We observed a general correlation between BioTracker hypoxia dye staining and Glut-1 expression in the μMeRe device, where more pronounced hypoxia levels were associated with greater increases in Glut-1 expression. Notably, the PC3 prostate cancer cell line was an outlier as it showed high BioTracker hypoxia dye fluorescence but did not alter Glut-1 expression. Interestingly, a cancer-specific relationship between hypoxia and Glut-1 upregulation has been reported in patient samples, where a high correlation was observed in bladder and colorectal cancers [61,62], while such correlation was weak or non-existent in cervical cancers [63,64]. Among ovarian cancers, expression of HIF-1α and Glut-1 varies based on the tumor subtype, with serous adenocarcinomas exhibiting higher levels of both markers than mucinous adenocarcinomas [65]. Furthermore, while media formulations can impact cell metabolism [66], they are not likely the main contributor to the heterogeneity in the metabolic rewiring behavior of the cancer cells observed in the assay. For instance, LNCaP and OAW42 cells were both cultured in RPMI media; however, only the LNCaP cells showed an increase in Glut-1 expression in the assay. Similarly, MCF7 and SKOV3 cells were both cultured in DMEM media, but an increase in Glut-1 expression was not observed for SKOV3 cells. Therefore, our results suggest that the intrinsic capability of specific cancer cells to drive hypoxia and undergo metabolic rewiring is the greater determinant of their rewiring behaviors.

Our RNA-seq analysis identified 5 DEGs that were shared across all the cell lines, including genes related to glycolysis and lipoprotein metabolism (*ALDOC, ANGPTL4, HK2*), hypoxia (*NDRG1*), and apoptosis (*BNIP3*). Patient data analyses indicated that these genes (except *HK2*) were clinically significant, as their high expression levels were associated with poorer survival outcomes and strongly correlated with the expression of 7 hypoxia genes in patient samples of ovarian, prostate, lung, and breast cancer. Notably, the clinical significance of these five genes has been reported by others in multiple cancer types originating from different organs [67–71], with variations among different cancer types. For instance, *NDRG1* overexpression is associated with poor clinical outcomes in triple-negative breast cancer patients, while the down-regulation of *NDRG1* is associated with poor clinical outcomes in gastric cancer patients [70]. Similar observations were made for *BNIP3* expression, where poor prognosis was associated with *BNIP3* regulation in patients with breast cancer and with *BNIP3* downregulation in patients with low-grade glioma [71]. The *HK2* expression was an outlier in the pooled survival analysis as its expression level did not correlate with patient outcomes. In agreement with our findings, it has been reported that the association between *HK2* expression levels and patient outcomes is cancer-specific. In a pan-cancer analysis of 33 different tumor types, including patient samples of ovarian, prostate, lung, and breast cancer, researchers observed no significant correlation between *HK2* gene expression and survival prognosis in 26 tumor types, while significant positive and negative correlations were found in the other 1 and 6 tumor types, respectively [72]. Overall, this is the first study to collectively identify these five genes as common indicators of hypoxia-associated metabolic rewiring behavior.

Using a genetically encoded hypoxia biosensor, we assessed the differences in HIF-1 signaling activity in cancer cells with distinct MeRe scores (LNCaP and SKOV3). Distinct HIF responses were observed between the two cancer cell lines, including the different oxygen thresholds that trigger their HIF-1 activity and the varying magnitudes of HIF response at 1% O_2. Furthermore, differential ROS levels were observed between the two cancer cells under hypoxia. Studies have shown that hypoxia-induced release of ROS by complex III in the mitochondrial ETC serves as hypoxia signaling molecules that lead to the stabilization of HIF-1α [73,74]. Alternatively, HIF stabilization can also occur through a mitochondria-independent pathway by a direct inhibition of prolyl hydroxylase (PHD) [75,76]. Therefore, based on the differences in the hypoxia-induced ROS production between the two cancer cells, LNCaP cells may stabilize their HIF-1α through ROS signaling, while HIF stabilization in SKOV3 cells may have occurred through PHD inhibition. The distinct rewiring behaviors of LNCaP and SKOV3 cells may also be

assessed using in vivo tumor models, by correlating the hypoxia/glycolysis marker expression of the in vivo tumors with the results observed in our assay.

It is widely recognized that hypoxia can reduce the efficacy of chemo-, radio-, and immunotherapies [13]. To overcome chemotherapeutic resistance in hypoxic tumors, anti-hypoxic drugs that target HIF-1α and its downstream target (e.g., nitroglycerin), or hypoxia-activated prodrugs (e.g., tirapazamine) have been developed. Unfortunately, these therapies have shown limited success when co-administered with cisplatin in clinical trials [77,78]. We observed distinct hypoxia-induced ROS production behaviors between LNCaP and SKOV3 cells, which represent cancer cells with distinct metabolic rewiring behaviors (Fig. 5H–L). Inspired by this, we demonstrated an enhanced therapeutic efficacy of cisplatin with the combined treatment of atovaquone (ATO), a mitochondrial inhibitor recognized to reduce ROS production in hypoxic tumors. In patients treated with ATO, expression of ROS-associated gene signatures was decreased, suggesting that by alleviating hypoxia, ATO also helps mitigate hypoxia-induced ROS generation [45]. Notably, this is different from the conventional approach of utilizing ROS scavengers, which directly aims at neutralizing ROS regardless of the ROS-causing conditions (e.g., hypoxia). As a comparison, we have evaluated the role of a ROS scavenger, N-acetyl-L-cysteine (NAC), in the therapeutic response of LNCaP cells to cisplatin (Fig. S4). Interestingly, NAC protected LNCaP cells against cisplatin treatment in both the μMeRe and normoxia devices. These results are in line with previous publications [79,80]. The contrasting effects of reducing cellular ROS by ATO and NAC treatment highlight the complexity of ROS signaling in chemotherapy resistance and emphasize the importance of addressing the cause (i.e., hypoxia-mediated metabolic rewiring) instead of the outcome (i.e. the elevated ROS) in cisplatin resistance. Additional potential applications of our assay may include preclinical assessment of metabolism-targeting therapeutic strategies and characterizing personalized treatment options on patient biopsies.

Overall, our μMeRe assay provides a unique perspective for revealing the inter- and intra-tumoral heterogeneity in metabolic rewiring and therapeutic resistance in the context of hypoxic TME. It lays the foundation for designing more effective personalized cancer medicine aiming at metabolic rewiring in TME.

4. Materials and methods

4.1. Cell culture

The panel of cancer cells consists of 8 human cancer cell lines originating from 4 different organs. T47D, SKOV3, and MCF7 were purchased from ATCC. LNCaP, PC3, PC9, and A549 cells were a generous gift from the Lawrence J. Ellison Institute for Transformative Medicine of University of Southern California. OAW42 cells were a generous gift from Andrea Bild's lab at City of Hope. All cell lines were maintained in a humidified incubator at 37 °C with 5% CO_2. OAW42, PC9, and LNCaP cells were cultured in RPMI 1640 medium (Thermo Fisher, Waltham, MA) supplemented with 10% fetal bovine serum (FBS; Sigma-Aldrich, St. Louis, MO), 100 U mL^{-1} penicillin and 100 μg mL^{-1} streptomycin (1% P/S, Thermo Fisher, Waltham, MA). SKOV3, A549, MCF7, T47D, and PC3 cells were cultured in DMEM (Thermo Fisher, Waltham, MA) supplemented with 10% FBS and 1% P/S.

4.2. Microdevice design and fabrication

Microdevices were designed and prepared as previously described [27,81]. Briefly, the microdevice design featured a circular middle chamber lined with the PC film (McMaster-Carr, Elmhurst, IL) at the top and a glass substrate at the bottom (gap size of 120 μm). The middle chamber was surrounded by two microfluidic channels (1 mm width × 800 μm). The master molds for the μMeRe and normoxia devices were milled on a polycarbonate (PC) block and vapor-polished with methylene chloride in a chemical hood to facilitate PDMS molding and plasma bonding of the replicated PDMS devices on the glass slides. The PC mold of the μMeRe device was designed to account for the thickness of the PC film, which was added later to achieve equal dimensions between μMeRe and normoxia devices.

Sylgard 184 (Dow, Inc., Midland, MI) PDMS was mixed at a ratio of 10:1 (base:curing agent) and cured over the milled surface. Cured PDMS was peeled from the master mold, and the injection ports were punched out. To fabricate μMeRe devices, circles 6 mm in diameter were cut out of a 0.01-inch-thick PC film. The circular PC films were inked with a thin layer of uncured PDMS mixture (10:1, base:curing agent) and attached to the cell culture chamber of μMeRe device. The attached PC film was fixed onto the PDMS base by baking overnight at 65 °C. All devices were plasma-treated (model PDC-001-HP, Harrick Plasma, Ithaca, NY) for 60 s and bonded onto a clean glass slide for cell culture.

4.3. Microdevice cell culture

Microdevices were UV-sterilized prior to cell culture. A 0.01% poly-d-lysine (PDL; Advanced BioMatrix, Carlsbad, CA) solution (w/v in sterile deionized (DI) water) was injected into the middle chamber of the sterilized microdevice and incubated for 30 min at room temperature. The microdevices were then rinsed twice with sterile DI water and filled with phosphate-buffered saline (PBS; VWR; Radnor, PA) until cell seeding. Each cancer cell type was resuspended in culture medium and injected into the middle chamber at an initial seeding density of 60,000 cells per microdevice. Cells were allowed to attach in a humidified incubator at 37 °C and 5% CO_2 for 2 h. After confirming cell attachment, an additional culture medium was introduced through the side channels of the microdevice for continued incubation.

4.4. Exogeneous and endogenous hypoxia marker

After 20 h of culture, microdevices were gently flushed with sterile PBS through the side channels. The side channels were then aspirated and injected with BioTracker 520 Green Hypoxia Dye (Sigma-Aldrich, St. Louis, MO), a hypoxia-selective fluorescent probe, at 5 μM in cell culture medium, and incubated at 37 °C and 5% CO_2 for 1 h. Subsequently, the staining solution was removed, and microdevices were gently flushed with sterile PBS before introducing fresh culture medium. After 3 h of additional incubation, microdevices were imaged at 10 × magnification using a Nikon Ti-E inverted fluorescence microscope.

The same samples were subsequently used for glucose transporter 1 (Glut-1) immunostaining and 4′,6-diamidino-2-phenylindole (DAPI) nuclear counterstain. Rabbit monoclonal anti-glucose transporter 1 (ab115730, 1:200) (Abcam, Cambridge, MA) as the primary antibody and Alexa Fluor 647-conjugated donkey anti-rabbit antibody (1:500) (Invitrogen, Waltham, MA) as the secondary antibody were used for immunostaining. Microdevices were disassembled for immunostaining. Samples were fixed in 4% paraformaldehyde (PFA; Electron Microscopy Sciences, Hatfield, PA) for 15 min, permeabilized in 0.1% Triton X-100 (Thermo Fisher, Waltham, MA) for 15 min, and blocked with 4% bovine serum albumin (BSA; HyClone, Logan, UT) for 1 h. Samples were then incubated in primary antibody for 1 h, rinsed three times in PBS, and incubated with secondary antibody for 1 h at room temperature. Immunostained samples were mounted with FluoroGel II containing DAPI (Electron Microscopy Sciences, Hatfield, PA). Images were acquired at 10 × magnification on a Nikon Ti-E inverted fluorescent microscope.

4.5. RNA extraction and RT-qPCR

All cancer types were cultured in the microdevice (normoxia and μMeRe) for 24 h before device disassembly and RNA extraction. RNA was extracted using the RNeasy Plus Micro Kit (Qiagen, Germantown, MD) following the manufacturer's instructions. The concentration and

purity of the isolated RNA were determined by absorbance on a NanoDrop One Spectrophotometer & Qubit (Thermo Fisher, Waltham, MA). For real-time quantitative PCRs, RNA samples were reverse transcribed into cDNA with SuperScript IV VILO Master Mix (Thermo Fisher, Waltham, MA) on a T100 Thermal Cycler (Bio-Rad, Hercules, CA). The cDNA was amplified with TaqMan Universal Master Mix II (Thermo Fisher, Waltham, MA) on a CFX384 Touch Real-Time PCR Detection System (Bio-Rad, Hercules, CA) to assess the expression of selected metabolism-related gene candidates. Data were normalized against housekeeping genes (*β-actin*, *GAPDH*, and *18S rRNA*) and internal sample control (ΔΔCt method). The ΔΔCt values were plotted in $\log_2$ scale to assess gene expression changes.

4.6. Metabolic rewiring (MeRe) scoring

An aggregated metric, metabolic rewiring (MeRe) score, was established using the data obtained from fluorescence images (BioTracker 520 Green Hypoxia Dye and Glut-1 expression) and RT-qPCR (13 genes related to glycolysis, oxidative phosphorylation (OXPHOS), and mitochondrial electron transport chain (ETC)).

The fluorescence images were scored based on the following parameters: 1) the fold difference of fluorescence intensity at the center of the μMeRe device versus normoxia device, and 2) the radial distance from the center of the μMeRe (i.e., highest fluorescence intensity) to the point where the fluorescence intensity falls below 30% of the highest fluorescence intensity (i.e., cutoff distance). The fluorescence signal cutoff (i.e., 70% of the highest fluorescence) was selected to describe the region within the micropattern with high fluorescence intensity. The fold change of fluorescence intensity between cells cultured in μMeRe versus normoxia device was scored based on the magnitude of change as 0 (<1.5-fold increase), 1 (between 1.5- and 2- fold increase), or 2 (≥2-fold increase). The cutoff distance of fluorescence intensity within the μMeRe was scored as 0 (<1500 μm, which is $< \frac{1}{2}$ of the microdevice radius), 1 (between 1500 μm and 2250 μm, which is between $\frac{1}{2}$ and $\frac{3}{4}$ of the microdevice radius), or 2 (≥2250 μm, which is $> \frac{3}{4}$ of the microdevice radius).

The changes in the expression of each gene were converted to a gene expression score E_i as −2 (down-regulation with $|\log_2(\text{fold change})| \geq 1$), −1 (down-regulation with $|\log_2(\text{fold change})|$ between 0.5 and 1), 0 ($|\log_2(\text{fold change})|$ between 0 and 0.5), 1 (up-regulation with $|\log_2(\text{fold change})|$ between 0.5 and 1), or 2 (up-regulation with $|\log_2(\text{fold change})| \geq 1$). On the basis of the expected hypoxia-induced metabolic rewiring from OXPHOS to glycolysis, each gene was also assigned with a weight score W_i of −1 (genes related to OXPHOS or mitochondrial ETC) or 1 (genes related to glycolysis). Multiplying the direction of expression change (E_i) with its weight (W_i) indicates the metabolic shift from OXPHOS to glycolysis of the specific cancer type. The sum total MeRe score (fluorescence images and gene expression) describes the comprehensive magnitude of metabolic rewiring for each cancer cell line.

4.7. RNA sequencing and analysis

RNA sample quality control (QC), library preparation/QC, and sequencing were performed by Novogene (Novogene Corporation Inc, Sacramento, CA). Quality of the RNA was assessed using Agilent 2100 Bioanalyzer (Agilent Technologies, Santa Clara, CA). Only the RNA samples that passed the QC were used. Messenger RNA was purified from total RNA using poly-T oligo-attached magnetic beads. After fragmentation, the first strand cDNA was synthesized using random hexamer primers, followed by the second strand cDNA synthesis. The library was ready after end repair, A-tailing, adapter ligation, size selection, amplification, and purification. Libraries were constructed with the NEBNExt Ultra II library kit (New England BioLabs Inc, Ipswich, MA). The library was checked with Qubit and real-time PCR for quantification and bioanalyzer for size distribution detection. Sequencing was run on the Illumina NovaSeq 6000 S4 platform using NovaSeq PE150 strategy (pair-end 150 bp read length, 20 million reads per sample).

The following pipeline was built on Partek Flow Genomic Analysis software (Partek Inc, St. Louis, MO) for the analyses: (i) pre-alignment QA/QC, (ii) trim bases from both ends base on minimum quality level (Phred) of 20 and a minimum read length of 25, (iii) alignment of mRNA-seq reads to the hg38 human genome using STAR, (iv) post-alignment QA/QC, (v) quantification to annotation model (Partek E/M), (vi) noise reduction filter to exclude features where the maximum ≤20, (vii) upper-quartile normalization after adding 1.0, (viii) principal component analysis (PCA), (ix) differential analysis using gene specific analysis (GSA), and (x) hierarchical clustering heatmap. For the differential analysis, the transcriptome of each cancer type in the μMeRe device was compared to its normoxia microdevice cultured counterpart, and the differentially expressed genes (DEGs) were identified and filtered to include only the genes with $|\log_2(\text{fold change})| \geq 2.0$ and FDR cutoff = 0.05. The filtered DEGs were utilized for the pathway enrichment analysis. Based on the filtered gene set, enriched biological pathways were identified for each cancer type, and enrichment scores were obtained for pathways of interest. A correlation between the obtained enrichment scores and the MeRe scores was performed to evaluate the relevance of the MeRe scores.

The filtered DEGs of the cancer panel were also exported from Partek Flow and organized using R to visualize the shared and distinct DEGs across the different cancer cell lines (UpSet Plot [29]).

The normalized data from Partek Flow were uploaded to Qiagen Ingenuity Pathway Analysis (IPA) software to identify canonical pathways via comparison analysis. Comparative gene expression analysis was performed on the uploaded data for each cancer type. The following cutoff was set for the gene expression analysis: $|\log_2(\text{fold change})| \geq 1.5$ and FDR cutoff = 0.05. This cutoff ensured that there was an adequate number of observations to identify the distinct expression profile in each cancer type, while avoiding excessive restrictions. Comparison analysis was performed across the expression analyses to identify the canonical pathways and the associated Z-score and $-\log_{10}$(P value).

4.8. Patient data analysis

Patient data analysis was performed using the TCGA dataset. For survival analysis, the patient cohorts were divided into 25% quartiles according to expression level of the genes of interest. The hazard ratio (HR) and P value were calculated based on Cox Proportional-Hazards (PH) Model. Pairwise Pearson correlation was used to estimate the relative expression levels of the 5-gene signature in hypoxia or normoxia tumors as distinguished by the expression level of the 7-gene hypoxia signature according to the literature [32–34]. Both Kaplan-Meier survival curves and Pearson correlation plots were directly retrieved from Gene Expression Profiling Interactive Analysis portal [82] without further processing.

4.9. Cell culture in an oxygen-controlled incubator

Heracell VIOS 160i Tri-gas CO_2 incubator (ThermoFisher, Waltham, MA) was used to generate culture conditions at specific oxygen levels. O_2 concentration in the incubator was established by continuously injecting N_2 gas until the target oxygen level was reached. The set oxygen level was allowed to stabilize overnight before cell culture. Microdevices without oxygen barriers (i.e., oxygen-permeable "normoxia" microdevices) were utilized in all experiments involving the hypoxia incubator. Initially, cancer cells were seeded in the normoxia device and were allowed to attach in a standard incubator at 37 °C, atmospheric O_2 level (21%), and 5% CO_2 for 2 h. After confirming cell attachment, microdevices were transferred to the hypoxia incubator for continued culture. Cells cultured at atmospheric O_2 level (21%) remained in the

standard incubator. CO_2 levels were maintained at 5% for all culture conditions.

4.10. Genetically encoded hypoxia sensors

Gene templates of the hypoxia reporter were constructed using polymerase chain reaction (PCR) amplification of the complementary DNA of a 5 repeat Hypoxia Response Elements (HRE) connected 5' to a minimal CMV promoter, UnaG, and PEST [24]. PCR was performed using synthesized primers (Integrated DNA Technologies) and Q5 DNA polymerase (NEB, M0491). The amplified gene elements were cloned into the modified pHR lentiviral transfer vector (pHR-PGK-mCherry), a gift from Wendell Lim (Addgene plasmid # 79124) digested using *Eco*RI, using Gibson Assembly (NEB, E2611L). A truncated CD19 (tCD19) fragment was also obtained to replace the mCherry component as a constitutive marker when needed. The constructed plasmid sequences were verified by Sanger sequencing (Genewiz).

SKOV3 and LNCaP cells were equipped with the hypoxia reporter through lentiviral transduction. Lentiviruses were produced from Lenti-X 293T cells (Clontech Laboratories, #632180) co-transfected with a pHR containing hypoxia reporter and the viral packaging plasmids pMD2.G and psPAX2 using the ProFection Mammalian Transfection System (Promega, Cat. No. E1200). Viral medium/supernatant was collected 48 h after transfection, filtered with 0.45 μm filter (Sigma-Millipore), and concentrated using PEG-it virus precipitation solution (System Biosciences, Cat. # LV825A-1). The virus titer was measured by flow cytometry. To generate the reporter-expressing cells, the concentrated virus was added with MOI of 1 into the cells, which were seeded with a density of 1×10^5 cells in a 6-well plate a day before transduction.

Cells containing hypoxia reporter were sorted by fluorescence-activated cell sorting (FACS; SONY SH800), three days post-transduction based on their constitutive marker (tCD19). tCD19 staining for flow cytometry was performed using Alexa Fluor® 647 anti-human CD19 Antibody (Clone: SJ25C1) according to the manufacturer's protocols (BioLegend 302220). Briefly, cells were washed and resuspended in PBS containing antibodies, incubated in the dark at room temperature, and washed three times before flow cytometry analysis and FACS. Gating was based on non-engineered cells with the same staining. Flow cytometry data were analyzed using FlowJo software (FlowJo).

4.11. Hypoxia-induced changes in mitochondrial reactive oxygen species

Cancer cells were seeded and cultured in the specified microdevice/oxygen conditions for 24 h before staining. Microdevices were gently flushed with sterile PBS and loaded with 10 μM CM-H_2DCFDA (Thermo Fisher, Waltham, MA) in sterile PBS to measure reactive oxygen species production. After 30 min of incubation, the staining solution was removed from the microdevices and filled with a culture medium before imaging. A working solution of CM-H_2DCFDA was prepared following the manufacturer's instructions.

4.12. Response to mitochondrial inhibition

After 12 h of culturing the cancer cells in the microdevice, the cell culture medium in the microdevice was replaced with either a medium containing 40 μM atovaquone (ATO) or a medium containing an equal volume of solvent (i.e., DMSO) before being incubated for another 12 h. The microdevices were stained for imaging (BioTracker hypoxia dye followed by Glut-1) or disassembled for RNA extraction. RT-qPCR was performed on the extracted RNA (using the same 13 genes related to glycolysis, OXPHOS, and mitochondrial ETC) to observe gene expression changes with and without ATO treatment.

4.13. Evaluation of therapy response (cisplatin and atovaquone)

For combination therapy with mitochondrial inhibition and cisplatin, three treatment conditions were evaluated using the microdevices: control (DMSO and water), 500 μM cisplatin, and pre-administration of 40 μM atovaquone followed by a combined treatment of 40 μM atovaquone and 500 μM cisplatin. To measure the therapy response, all devices were disassembled and stained with 1 μM calcein-AM and 1 μM propidium iodide for 30 min at room temperature before imaging.

4.14. Image analysis

Images were processed and quantified with ImageJ software (NIH, Bethesda, MD), and the obtained data were plotted using Prism 10 (GraphPad Software, Inc., San Diego, CA). The fluorescence intensity of the staining was binned radially in concentric circles from the center of the cancer micropattern.

For the analysis of BioTracker hypoxia dye, fluorescence fold change was obtained by dividing the fluorescence intensity obtained from the center of the μMeRe micropattern by the fluorescence intensity obtained from the center of normoxia micropattern counterpart. For the analysis of Glut-1, the fluorescence intensity was first normalized by dividing the total fluorescence intensity by the number of cells counted in each spatial region. Cutoff distance (i.e., distance from the center to the point where the fluorescence intensity falls to 70% of the fluorescence observed at the center) for both BioTracker hypoxia dye and Glut-1 staining was obtained by interpolating a nonlinear curve fit, generated using Boltzmann sigmoidal equation. This curve was generated based on the fluorescence intensity observed along the radius of the μMeRe micropattern.

For the analysis of UnaG and CM-H_2DCFDA, the change in fluorescence intensity between the cancer cells cultured in the μMeRe device vs. normoxia microdevice and 1% O_2 vs. 21% O_2 incubator was obtained by subtracting the fluorescence intensity obtained from the center of the cancer micropattern in each culture condition. The oxygen-threshold level, defined as the point where the UnaG fluorescence intensity reaches 50% of the maximum measured fluorescence, was determined by interpolating a nonlinear curve fit using the Boltzmann sigmoidal equation. This curve was constructed based on the measured UnaG fluorescence intensity at each oxygen concentration.

For the cancer therapy evaluation, the areal density of living cells (positive calcein signal) was used to indicate cancer cell survival, as many of the dead cells were washed away during the live/dead staining. For the live areal density, the areal density of the treated cancer micropattern was divided by the areal density of the untreated/control cancer micropattern.

4.15. Statistical analysis

All statistical analyses were performed using Prism 10 (GraphPad Software, Inc., San Diego, CA). All data were presented in mean ± standard deviation (SD), as stated in the figure legends. For pairwise comparisons, Student's t-test was used. For the analysis of UnaG fluorescence intensities of LNCaP and SKOV3 cells under various oxygen levels, significance was assessed by two-way analysis of variance (ANOVA) followed by Šídák's multiple comparisons test. The figure highlights the comparison of mean fluorescence intensities between the two cell lines at each oxygen level. For the analysis of viability of LNCaP and SKOV3 cells under various cisplatin treatment conditions, significance was assessed by two-way ANOVA followed by Šídák's multiple comparisons test. The figure highlights the comparison of mean live areal density between cisplatin–μMeRe and ATO & cisplatin–μMeRe treatment conditions at each radial distance. Correlation analyses were conducted using Pearson r, and P values were tested with zero-slope hypothesis. For all data, P values were indicated as numbers or as n.s.

(not significant, $P > 0.05$) on the plots. For all analyses, $P < 0.05$ was considered significant.

CRediT authorship contribution statement

Jeong Min Oh: Writing – review & editing, Writing – original draft, Visualization, Methodology, Investigation, Formal analysis, Data curation, Conceptualization. **Tianze Guo:** Investigation. **Hydari Masuma Begum:** Investigation. **Saci-Elodie Marty:** Investigation, Data curation. **Liang Sha:** Investigation, Formal analysis. **Cem Kilic:** Formal analysis. **Hao Zhou:** Formal analysis. **Yali Dou:** Supervision. **Keyue Shen:** Writing – review & editing, Writing – original draft, Visualization, Supervision, Resources, Project administration, Methodology, Funding acquisition, Conceptualization.

Data and materials availability

All data needed to evaluate the conclusions in the paper are present in the paper and/or the Supplementary Materials. RNA-seq data are available from the NCBI GEO database, under the accession number GSE265781.

Ethics approval and consent to participate

Ethics approval and informed consent was not required for this study.

Funding

This work was supported by the USC Graduate School Provost Fellowship, USC Viterbi School of Engineering, a National Institutes of Health (NIH) grant R01CA220012, and a STOP CANCER Marni Levine Memorial Research Career Development Award. This research was also supported by shared resources from an NIH National Cancer Institute Award (P30CA014089).

Declaration of competing interest

K.S. is an inventor on a patent related to this work filed by University of Southern California (US10829730B2, filed on March 30, 2018, published on November 10, 2020). The authors declare no other competing interests.

Acknowledgements

We thank Dr. Friedemann Kiefer at the European Institute for Molecular Imaging for providing us with the hypoxia sensor constructs. We sincerely thank Meng Li at the University of Southern California Libraries Bioinformatics Service for providing help with RNA-seq data analysis.

Appendix A. Supplementary data

Supplementary data to this article can be found online at https://doi.org/10.1016/j.bioactmat.2025.02.030.

References

[1] N. Vasan, J. Baselga, D.M. Hyman, A view on drug resistance in cancer, Nature 575 (2019) 299–309.
[2] A. Morandi, S. Indraccolo, Linking metabolic reprogramming to therapy resistance in cancer, Biochim. Biophys. Acta Rev. Canc 1868 (2017) 1–6.
[3] A. Luengo, D.Y. Gui, M.G. Vander Heiden, Targeting metabolism for cancer therapy, Cell Chem. Biol. 24 (2017) 1161–1180.
[4] J. Kim, R.J. DeBerardinis, Mechanisms and implications of metabolic heterogeneity in cancer, Cell Metab. 30 (2019) 434–446.
[5] K. Ortmayr, S. Dubuis, M. Zampieri, Metabolic profiling of cancer cells reveals genome-wide crosstalk between transcriptional regulators and metabolism, Nat. Commun. 10 (2019) 1841.
[6] Y. Huang, V. Mohanty, M. Dede, K. Tsai, M. Daher, L. Li, K. Rezvani, K. Chen, Characterizing cancer metabolism from bulk and single-cell RNA-seq data using METAFlux, Nat. Commun. 14 (2023) 4883.
[7] P. Hai, T. Imai, S. Xu, R. Zhang, R.L. Aft, J. Zou, L.V. Wang, High-throughput, label-free, single-cell photoacoustic microscopy of intratumoral metabolic heterogeneity, Nat. Biomed. Eng. 3 (2019) 381–391.
[8] M. Demicco, X.-Z. Liu, K. Leithner, S.-M. Fendt, Metabolic heterogeneity in cancer, Nat. Metab. 6 (2024) 18–38.
[9] A.C. Gonçalves, E. Richiardone, J. Jorge, B. Polónia, C.P.R. Xavier, I.C. Salaroglio, C. Riganti, M.H. Vasconcelos, C. Corbet, A.B. Sarmento-Ribeiro, Impact of cancer metabolism on therapy resistance – clinical implications, Drug Resist. Updates 59 (2021) 100797.
[10] M. Redondo-Muñoz, F.J. Rodriguez-Baena, P. Aldaz, A. Caballé-Mestres, V. Moncho-Amor, M. Otaegi-Ugartemendia, E. Carrasco-Garcia, A. Olias-Arjona, I. Lasheras-Otero, E. Santamaria, A. Bocanegra, L. Chocarro, A. Grier, M. Dzieciatkowska M, C. Bigas, J. Martin, U. Urdiroz-Urricelqui, F. Marzo, E. Santamaria, G. Kochan, D. Escors, I.M. Larrayoz, H. Heyn, A. D'Alessandro, C.S.-O. Attolini, A. Matheu, C. Wellbrock, S.A. Benitah, B. Sanchez-Laorden, I. Arozarena, Metabolic rewiring induced by ranolazine improves melanoma responses to targeted therapy and immunotherapy, Nat. Metab. 5 (2023) 1544–1562.
[11] J.-C. Marine, S.-J. Dawson, M.A. Dawson, Non-genetic mechanisms of therapeutic resistance in cancer, Nat. Rev. Cancer 20 (2020) 743–756.
[12] R. Baumeister, C.T. Murphy, T. Heimbucher, Metabolic adaptation to hypoxia: do worms and cancer cells share common metabolic responses to hypoxic stress? Cell Death Differ. 28 (2021) 1434–1436.
[13] Z. Chen, F. Han, Y. Du, H. Shi, W. Zhou, Hypoxic microenvironment in cancer: molecular mechanisms and therapeutic interventions, Signal Transduct. Targeted Ther. 8 (2023) 70.
[14] Y. Ye, Q. Hu, H. Chen, K. Liang, Y. Yuan, Y. Xiang, H. Ruan, Z. Zhang, A. Song, H. Zhang, L. Liu, L. Diao, Y. Lou, B. Zhou, L. Wang, S. Zhou, J. Gao, E. Jonasch, S. H. Lin, Y. Xia, C. Lin, L. Yang, G.B. Mills, H. Liang, L. Han, Characterization of hypoxia-associated molecular features to aid hypoxia-targeted therapy, Nat. Metab. 1 (2019) 431–444.
[15] A. Emami Nejad, S. Najafgholian, A. Rostami, A. Sistani, S. Shojaeifar, M. Esparvarinha, R. Nedaeinia, S. Haghjooy Javanmard, M. Taherian, M. Ahmadlou, R. Salehi, B. Sadeghi, M. Manian, The role of hypoxia in the tumor microenvironment and development of cancer stem cell: a novel approach to developing treatment, Cancer Cell Int. 21 (2021) 62.
[16] T. Hompland, C.S. Fjeldbo, H. Lyng, Tumor hypoxia as a barrier in cancer therapy: why levels matter, Cancers 13 (2021) 499.
[17] S.J. Kierans, C.T. Taylor, Regulation of glycolysis by the hypoxia-inducible factor (HIF): implications for cellular physiology, J. Physiol. 599 (2021) 23–37.
[18] S.C.-E.S. Lee, A.H.A. Pyo, M. Koritzinsky, Longitudinal dynamics of the tumor hypoxia response: from enzyme activity to biological phenotype, Sci. Adv. 9 (2023) eadj6409.
[19] E. Andreucci, S. Peppicelli, J. Ruzzolini, F. Bianchini, A. Biagioni, L. Papucci, L. Magnelli, B. Mazzanti, B. Stecca, L. Calorini, The acidic tumor microenvironment drives a stem-like phenotype in melanoma cells, J. Mol. Med. (Berl.) 98 (2020) 1431–1446.
[20] X. Jing, F. Yang, C. Shao, K. Wei, M. Xie, H. Shen, Y. Shu, Role of hypoxia in cancer therapy by regulating the tumor microenvironment, Mol. Cancer 18 (2019) 157.
[21] V. Petrova, M. Annicchiarico-Petruzzelli, G. Melino, I. Amelio, The hypoxic tumour microenvironment, Oncogenesis 7 (2018) 10.
[22] Z.E. Stine, Z.T. Schug, J.M. Salvino, C.V. Dang, Targeting cancer metabolism in the era of precision oncology, Nat. Rev. Drug Discov. 21 (2022) 141–162.
[23] C.G. Hubert, M. Rivera, L.C. Spangler, Q. Wu, S.C. Mack, B.C. Prager, M. Couce, R. E. McLendon, A.E. Sloan, J.N. Rich, A three-dimensional organoid culture system derived from human glioblastomas recapitulates the hypoxic gradients and cancer stem cell heterogeneity of tumors found in vivo, Cancer Res. 76 (2016) 2465–2477.
[24] J.A. Ju, I. Godet, I.C. Ye, J. Byun, H. Jayatilaka, S.J. Lee, L. Xiang, D. Samanta, M. H. Lee, P.-H. Wu, D. Wirtz, G.L. Semenza, D.M. Gilkes, Hypoxia selectively enhances integrin α5β1 receptor expression in breast cancer to promote metastasis, Mol. Cancer Res. 15 (2017) 723–734.
[25] B. Horst, S. Pradhan, R. Chaudhary, E. Listik, L. Quintero-Macias, A.S. Choi, M. Southard, Y. Liu, R. Whitaker, N. Hempel, A. Berchuck, A.B. Nixon, N.Y. Lee, Y. I. Henis, K. Mythreye, Hypoxia-induced inhibin promotes tumor growth and vascular permeability in ovarian cancers, Commun. Biol. 5 (2022) 536.
[26] S.J. Han, S. Kwon, K.S. Kim, Challenges of applying multicellular tumor spheroids in preclinical phase, Cancer Cell Int. 21 (2021) 152.
[27] J.M. Oh, H.M. Begum, Y.L. Liu, Y. Ren, K. Shen, Recapitulating tumor hypoxia in a cleanroom-free, liquid-pinning-based microfluidic tumor model, ACS Biomater. Sci. Eng. 8 (2022) 3107–3121.
[28] D.P. Yen, Y. Ando, K. Shen, A Cost-Effective micromilling platform for Rapid Prototyp.Microdevices.Technol. 4 (2016) 234–239.
[29] A. Lex, N. Gehlenborg, H. Strobelt, R. Vuillemot, H. Pfister, UpSet: visualization of intersecting sets, IEEE Trans. Vis. Comput. Graph. 20 (2014) 1983–1992.
[30] L. Sha, Z. Yang, S. An, W. Yang, S. Kim, H. Oh, J. Xu, J. Yin, H. Wang, H.-J. Lenz, W. An, U.-S. Cho, Y. Dou, Non-canonical MLL1 activity regulates centromeric phase separation and genome stability, Nat. Cell Biol. 25 (2023) 1637–1649.
[31] J. Lukovic, K. Han, M. Pintilie, N. Chaudary, R.P. Hill, A. Fyles, M. Milosevic, Intratumoral heterogeneity and hypoxia gene expression signatures: is a single biopsy adequate? Clin. Transl. Radiat. Oncol. 19 (2019) 110–115.

[32] Q. Zhang, R. Huang, H. Hu, L. Yu, Q. Tang, Y. Tao, Z. Liu, J. Li, G. Wang, Integrative analysis of hypoxia-associated signature in pan-cancer, iScience 23 (2020).

[33] B. Lane, M.T. Khan, A. Choudhury, A. Salem, C.M.L. West, Development and validation of a hypoxia-associated signature for lung adenocarcinoma, Sci. Rep. 12 (2022) 1290.

[34] R. Abou Khouzam, S.P. Rao, G.H. Venkatesh, N.A. Zeinelabdin, S. Buart, M. Meylan, M. Nimmakayalu, S. Terry, S. Chouaib, An eight-gene hypoxia signature predicts survival in pancreatic cancer and is associated with an immunosuppressed tumor microenvironment, Front. Immunol. 12 (2021).

[35] A. Krämer, J. Green, J. Pollard Jr., S. Tugendreich, Causal analysis approaches in ingenuity pathway analysis, Bioinformatics 30 (2014) 523–530.

[36] L.E. Huang, Z. Arany, D.M. Livingston, H.F. Bunn, Activation of hypoxia-inducible transcription factor depends primarily upon redox-sensitive stabilization of its α subunit *, J. Biol. Chem. 271 (1996) 32253–32259.

[37] R. Erapaneedi, V.V. Belousov, M. Schäfers, F. Kiefer, A novel family of fluorescent hypoxia sensors reveal strong heterogeneity in tumor hypoxia at the cellular level, EMBO J. 35 (2016) 102–113.

[38] D. Hanahan, Hallmarks of cancer: new dimensions, Cancer Discov. 12 (2022) 31–46.

[39] G.B. Waypa, K.A. Smith, P.T. Schumacker, O2 sensing, mitochondria and ROS signaling: the fog is lifting, Mol. Aspect. Med. 47–48 (2016) 76–89.

[40] H.J. Jung, J.S. Shim, J. Lee, Y.M. Song, K.C. Park, S.H. Choi, N.D. Kim, J.H. Yoon, P.T. Mungai, P.T. Schumacker, H.J. Kwon, Terpestacin inhibits tumor angiogenesis by targeting UQCRB of mitochondrial complex III and suppressing hypoxia-induced reactive oxygen species production and cellular oxygen sensing *</sup>, J. Biol. Chem. 285 (2010) 11584–11595.

[41] A.L. Orr, L. Vargas, C.N. Turk, J.E. Baaten, J.T. Matzen, V.J. Dardov, S.J. Attle, J. Li, D.C. Quackenbush, R.L.S. Goncalves, I.V. Perevoshchikova, H.M. Petrassi, S. L. Meeusen, E.K. Ainscow, M.D. Brand, Suppressors of superoxide production from mitochondrial complex III, Nat. Chem. Biol. 11 (2015) 834–836.

[42] S. Dasari, P. Bernard Tchounwou, Cisplatin in cancer therapy: molecular mechanisms of action, Eur. J. Pharmacol. 740 (2014) 364–378.

[43] N. Devarajan, R. Manjunathan, S.K. Ganesan, Tumor hypoxia: the major culprit behind cisplatin resistance in cancer patients, Crit. Rev. Oncol. Hematol. 162 (2021) 103327.

[44] T.M. Ashton, E. Fokas, L.A. Kunz-Schughart, L.K. Folkes, S. Anbalagan, M. Huether, C.J. Kelly, G. Pirovano, F.M. Buffa, E.M. Hammond, M. Stratford, R.J. Muschel, G. S. Higgins, W.G. McKenna, The anti-malarial atovaquone increases radiosensitivity by alleviating tumour hypoxia, Nat. Commun. 7 (2016) 12308.

[45] M. Skwarski, D.R. McGowan, E. Belcher, F. Di Chiara, D. Stavroulias, M. McCole, J. L. Derham, K.-Y. Chu, E. Teoh, J. Chauhan, D. O'Reilly, B.H.L. Harris, P.S. Macklin, J.A. Bull, M. Green, G. Rodriguez-Berriguete, R. Prevo, L.K. Folkes, L. Campo, P. Ferencz, P.L. Croal, H. Flight, C. Qi, J. Holmes, J.P.B. O'Connor, F.V. Gleeson, W. G. McKenna, A.L. Harris, D. Bulte, F.M. Buffa, R.E. Macpherson, G.S. Higgins, Mitochondrial inhibitor atovaquone increases tumor oxygenation and inhibits hypoxic gene expression in patients with non–small cell lung cancer, Clin. Cancer Res. 27 (2021) 2459–2469.

[46] D.C. Singleton, A. Macann, W.R. Wilson, Therapeutic targeting of the hypoxic tumour microenvironment, Nat. Rev. Clin. Oncol. 18 (2021) 751–772.

[47] H.-C. Shih, T.-A. Lee, H.-M. Wu, P.-L. Ko, W.-H. Liao, Y.-C. Tung, Microfluidic collective cell migration assay for study of endothelial cell proliferation and migration under combinations of oxygen gradients, tensions, and drug treatments, Sci. Rep. 9 (2019) 8234.

[48] N. Takahashi, D. Yoshino, R. Sugahara, S. Hirose, K. Sone, J.-P. Rieu, K. Funamoto, Microfluidic platform for the reproduction of hypoxic vascular microenvironments, Sci. Rep. 13 (2023) 5428.

[49] I. Martínez-Reyes, N.S. Chandel, Cancer metabolism: looking forward, Nat. Rev. Cancer 21 (2021) 669–680.

[50] F. Zhang, Y. Ma, D. Li, J. Wei, K. Chen, E. Zhang, G. Liu, X. Chu, X. Liu, W. Liu, X. Tian, Y. Yang, Cancer associated fibroblasts and metabolic reprogramming: unraveling the intricate crosstalk in tumor evolution, J. Hematol. Oncol. 17 (2024) 80.

[51] F. Danzi, R. Pacchiana, A. Mafficini, M.T. Scupoli, A. Scarpa, M. Donadelli, A. Fiore, To metabolomics and beyond: a technological portfolio to investigate cancer metabolism, Signal Transduct. Targeted Ther. 8 (2023) 137.

[52] S.V. Puram, I. Tirosh, A.S. Parikh, A.P. Patel, K. Yizhak, S. Gillespie, C. Rodman, C. L. Luo, E.A. Mroz, K.S. Emerick, D.G. Deschler, M.A. Varvares, R. Mylvaganam, O. Rozenblatt-Rosen, J.W. Rocco, W.C. Faquin, D.T. Lin, A. Regev, B.E. Bernstein, Single-cell transcriptomic analysis of primary and metastatic tumor ecosystems in head and neck cancer, Cell 171 (2017) 1611–1624.e1624.

[53] R.J. Argüello, A.J. Combes, R. Char, J.-P. Gigan, A.I. Baaziz, E. Bousiquot, V. Camosseto, B. Samad, J. Tsui, P. Yan, S. Boissonneau, D. Figarella-Branger, E. Gatti, E. Tabouret, M.F. Krummel, P. Pierre, SCENITH: a flow cytometry-based method to functionally profile energy metabolism with single-cell resolution, Cell Metab. 32 (2020) 1063–1075.e1067.

[54] S. Kjølle, K. Finne, E. Birkeland, V. Ardawatia, I. Winge, S. Aziz, G. Knutsvik, E. Wik, J.A. Paulo, H. Vethe, D. Kleftogiannis, L.A. Akslen, Hypoxia induced responses are reflected in the stromal proteome of breast cancer, Nat. Commun. 14 (2023) 3724.

[55] M.S. Zhang, J.D. Cui, D. Lee, V.W.-H. Yuen, D.K.-C. Chiu, C.C. Goh, J.W.-S. Cheu, A.P.-W. Tse, M.H.-R. Bao, B.P.Y. Wong, C.Y. Chen, C.-M. Wong, I.O.-L. Ng, C.C.-L. Wong, Hypoxia-induced macropinocytosis represents a metabolic route for liver cancer, Nat. Commun. 13 (2022) 954.

[56] K. Saxena, M.K. Jolly, Acute vs. Chronic vs. Cyclic hypoxia: their differential dynamics, molecular mechanisms, and effects on tumor progression, Biomolecules 9 (2019) 339.

[57] A.D. Midha, Y. Zhou, B.B. Queliconi, A.M. Barrios, A.G. Haribowo, B.T.L. Chew, C. O.Y. Fong, J.E. Blecha, H. VanBrocklin, Y. Seo, I.H. Jain, Organ-specific fuel rewiring in acute and chronic hypoxia redistributes glucose and fatty acid metabolism, Cell Metab. 35 (2023) 504–516.e505.

[58] T. Uchida, F. Rossignol, M.A. Matthay, R. Mounier, S. Couette, E. Clottes, C. Clerici, Prolonged hypoxia differentially regulates hypoxia-inducible factor (HIF)-1α and HIF-2α expression in lung epithelial cells: implication of natural antisense HIF-1α *, J. Biol. Chem. 279 (2004) 14871–14878.

[59] K.C. Carvalho, I.W. Cunha, R.M. Rocha, F.R. Ayala, M.M. Cajaíba, M.D. Begnami, R.S. Vilela, G.R. Paiva, R.G. Andrade, F.A. Soares, GLUT1 expression in malignant tumors and its use as an immunodiagnostic marker, Clinics 66 (2011) 965–972.

[60] Dania C. Liemburg-Apers, Tom J.J. Schirris, Frans G.M. Russel, Peter H.G. M. Willems, Werner J.H. Koopman, Mitoenergetic dysfunction triggers a rapid compensatory increase in steady-state glucose flux, Biophys. J. 109 (2015) 1372–1386.

[61] P.J. Hoskin, A. Sibtain, F.M. Daley, G.D. Wilson, GLUT1 and CAIX as intrinsic markers of hypoxia in bladder cancer: relationship with vascularity and proliferation as predictors of outcome of ARCON, Br. J. Cancer 89 (2003) 1290–1297.

[62] F.-Y. Chung, M.-Y. Huang, C.-S. Yeh, H.-J. Chang, T.-L. Cheng, L.-C. Yen, J.-Y. Wang, S.-R. Lin, GLUT1 gene is a potential hypoxic marker in colorectal cancer patients, BMC Cancer 9 (2009) 241.

[63] A. Mayer, M. Höckel, A. Wree, P. Vaupel, Microregional expression of glucose transporter-1 and oxygenation status: lack of correlation in locally advanced cervical cancers, Clin. Cancer Res. 11 (2005) 2768–2773.

[64] R. Airley, J. Loncaster, S. Davidson, M. Bromley, S. Roberts, A. Patterson, R. Hunter, I. Stratford, C. West, Glucose transporter glut-1 expression correlates with tumor hypoxia and predicts metastasis-free survival in advanced carcinoma of the Cervix1, Clin. Cancer Res. 7 (2001) 928–934.

[65] T. Iida, M. Yasuda, M. Miyazawa, M. Fujita, R.Y. Osamura, T. Hirasawa, T. Muramatsu, M. Murakami, K. Saito, M. Mikami, Hypoxic status in ovarian serous and mucinous tumors: relationship between histological characteristics and HIF-1α/GLUT-1 expression, Arch. Gynecol. Obstet. 277 (2008) 539–546.

[66] T. Ackermann, S. Tardito, Cell culture medium formulation and its implications in cancer metabolism, Trends Cancer 5 (2019) 329–332.

[67] Y.-C. Chang, Y.-C. Yang, C.-P. Tien, C.-J. Yang, M. Hsiao, Roles of aldolase family genes in human cancers and diseases, Trends Endocrinol. Metabol. 29 (2018) 549–559.

[68] L. La Paglia, A. Listì, S. Caruso, V. Amodeo, F. Passiglia, V. Bazan, D. Fanale, Potential role of ANGPTL4 in the cross talk between metabolism and cancer through PPAR signaling pathway, PPAR Res. 2017 (2017) 8187235.

[69] Y. Liu, K. Wu, L. Shi, F. Xiang, K. Tao, G. Wang, Prognostic significance of the metabolic marker hexokinase-2 in various solid tumors: a meta-analysis, PLoS One 11 (2016) e0166230.

[70] S. Ghafouri-Fard, S. Ahmadi Teshnizi, B.M. Hussen, M. Taheri, G. Sharifi, A review on the role of NDRG1 in different cancers, Mol. Biol. Rep. 50 (2023) 6251–6264.

[71] Q. Yu, W. Fu, Y. Fu, W. Ye, H. Yan, Z. Yu, R. Li, Y. Cai, Y. Chen, L. Wang, X. Wei, Y. Chen, Y. Zhang, H. Ying, F. Tang, F. Dai, W. Han, BNIP3 as a potential biomarker for the identification of prognosis and diagnosis in solid tumours, Mol. Cancer 22 (2023) 143.

[72] R. Li, S. Mei, Q. Ding, Q. Wang, L. Yu, F. Zi, A pan-cancer analysis of the role of hexokinase II (HK2) in human tumors, Sci. Rep. 12 (2022) 18807.

[73] E.L. Bell, T.A. Klimova, J. Eisenbart, C.T. Moraes, M.P. Murphy, G.R.S. Budinger, N.S. Chandel, The Qo site of the mitochondrial complex III is required for the transduction of hypoxic signaling via reactive oxygen species production, JCB (J. Cell Biol.) 177 (2007) 1029–1036.

[74] R.D. Guzy, P.T. Schumacker, Oxygen sensing by mitochondria at complex III: the paradox of increased reactive oxygen species during hypoxia, Exp. Physiol. 91 (2006) 807–819.

[75] E.C. Vaux, E. Metzen, K.M. Yeates, P.J. Ratcliffe, Regulation of hypoxia-inducible factor is preserved in the absence of a functioning mitochondrial respiratory chain, Blood 98 (2001) 296–302.

[76] R.D. Guzy, B. Hoyos, E. Robin, H. Chen, L. Liu, K.D. Mansfield, M.C. Simon, U. Hammerling, P.T. Schumacker, Mitochondrial complex III is required for hypoxia-induced ROS production and cellular oxygen sensing, Cell Metab. 1 (2005) 401–408.

[77] P.A. DiSilvestro, S. Ali, P.S. Craighead, J.A. Lucci, Y.C. Lee, D.E. Cohn, N. M. Spirtos, K.S. Tewari, C. Muller, W.H. Gajewski, M.M. Steinhoff, B.J. Monk, Phase III randomized trial of weekly cisplatin and irradiation versus cisplatin and tirapazamine and irradiation in stages IB2, IIA, IIB, IIIB, and IVA cervical carcinoma limited to the pelvis: a Gynecologic Oncology Group study, J. Clin. Oncol. 32 (2014) 458–464.

[78] M. Meunier, A. Yammine, A. Bettaieb, S. Plenchette, Nitroglycerin: a comprehensive review in cancer therapy, Cell Death Dis. 14 (2023) 323.

[79] C. Sun, E. Guo, B. Zhou, W. Shan, J. Huang, D. Weng, P. Wu, C. Wang, S. Wang, W. Zhang, Q. Gao, X. Xu, B. Wang, J. Hu, D. Ma, G. Chen, A reactive oxygen species scoring system predicts cisplatin sensitivity and prognosis in ovarian cancer patients, BMC Cancer 19 (2019) 1061.

[80] D.-F. Xue, S.-T. Pan, G. Huang, J.-X. Qiu, ROS enhances the cytotoxicity of cisplatin by inducing apoptosis and autophagy in tongue squamous cell carcinoma cells, Int. J. Biochem. Cell Biol. 122 (2020) 105732.
[81] J.M. Oh, K. Shen, Cleanroom-free microfluidic device for natural induction of hypoxia in 2D and 3D tumor models, in: D.M. Gilkes (Ed.), Hypoxia: Methods and Protocols, Springer US, New York, NY, 2024, pp. 227–247.
[82] Z. Tang, B. Kang, C. Li, T. Chen, Z. Zhang, GEPIA2: an enhanced web server for large-scale expression profiling and interactive analysis, Nucleic Acids Res. 47 (2019) W556–W560.